



# Experimental investigation on the turbulent wake flow in fully established transonic buffet conditions

Christopher Julian Schauerte<sup>1</sup> · Anne-Marie Schreyer<sup>1</sup>

Received: 15 January 2023 / Revised: 30 August 2023 / Accepted: 4 October 2023 / Published online: 2 November 2023  
© The Author(s) 2023

## Abstract

The transonic flight regime is often dominated by transonic buffet, a highly unsteady and complex shock-wave/boundary-layer interaction involving major parts of the flow field. The phenomenon is associated with a large-amplitude periodic motion of the compression shock coupled with large-scale flow separation and intermittent re-attachment. Due to the resulting large-scale variation of the global flow topology, also the turbulent wake of the airfoil or wing is severely affected, and so are any aerodynamic devices downstream on which the wake impinges. To analyze and understand the turbulent structures and dynamics of the wake, we performed a comprehensive experimental study of the near wake of the supercritical OAT15A airfoil in transonic buffet conditions at a chord Reynolds number of  $2 \times 10^6$ . Velocity field measurements reveal severe global influences of the buffet mode on both the surface-bound flow field on the suction side of the airfoil and the wake. The flow is intermittently strongly separated, with a significant momentum deficit that extends far into the wake. The buffet motion induces severe disturbances and variations of the turbulent flow, as shown on the basis of phase-averaged turbulent quantities in terms of Reynolds shear stress and RMS-values. The spectral nature of downstream-convecting fluctuations and turbulent structures are analyzed using high-speed focusing schlieren sequences. Analyses of the power spectral density pertaining to the vortex shedding in the direct vicinity of the trailing edge indicate dominant frequencies one order of magnitude higher than those associated with shock buffet ( $St_c = \mathcal{O}(1)$ ) vs.  $St_c = \mathcal{O}(0.1)$ ). It is shown that the flapping motion of the shear layer is accompanied by the formation of a von Kármán-type vortex street of fluctuating strength. These wake structures and dynamics will impact any downstream aerodynamic devices affected by the wake. Our study, therefore, allows conclusions regarding the incoming flow of devices such as the tail plane.

**Keywords** Transonic buffet · Airfoil · Supercritical · Shock wave · SWBLI · Turbulent flow · Wake · Vortex shedding

## 1 Introduction

The transonic flight regime is often characterized by the occurrence of local supersonic regions on the suction side of airfoils and wings, which are terminated by a shock wave [1]. For sufficiently strong interactions, shock-induced flow separation may span the entire region from the shock to the trailing edge [2]. For certain combinations of Mach number, Reynolds number, and angle of attack, the transonic flow about the airfoil becomes unsteady, and the compression

shock and separated boundary layer carry out periodic oscillations [1]. The resulting complex shock-wave/boundary-layer interaction involves major parts of the flow field [3] and is typically referred to as transonic buffet. The self-sustained dynamic back-and-forth motion of the shock wave is accompanied by strong variations of the shock strength, thus inciting a periodic thickening and shrinking of the separated shear layer [4]. This self-excited periodic phenomenon is, inter alia, associated with a highly unsteady flow field [2], which results in low-frequency fluctuation of the integral aerodynamic quantities, i.e. the lift and drag coefficients [5, 6].

For specific frequencies of this periodic change between a severely separated boundary layer and periods of mostly reattached flow, the aerodynamic phenomenon and the aircraft structure may interact. This mechanical coupling with the airframe can lead to a resonance of the wing (the

✉ Christopher Julian Schauerte  
c.schauerte@aia.rwth-aachen.de

Anne-Marie Schreyer  
a.schreyer@aia.rwth-aachen.de

<sup>1</sup> Institute of Aerodynamics, RWTH Aachen University,  
Wüllnerstraße 5a, 52062 Aachen, NW, Germany

so-called buffeting), inciting a potentially deleterious effect on the structural integrity [5, 6].

As the buffet onset constrains the usable range of the flight envelope [2, 6], its understanding is one of the major challenges in the design of modern civil aircraft [7, 8]. The number of applications of supercritical airfoils increases with the increasing demand for fast air travel. Therefore, the overall efficiency of modern civil aircraft becomes more and more relevant and the significance of a thorough understanding of the buffet phenomenon increases, as it is a prerequisite to identify and potentially shift the limits of the flight envelope.

Several possible explanations for the underlying mechanisms of this oscillatory shock motion have been suggested. For flow configurations with large wake fluctuations in the context of unsteady shock motion, Lee et al. [9] studied the formation of upstream traveling waves. These waves were advanced as an essential element to predict the periodic shock oscillation [10]. Tijdeman [11] interpreted these waves as an immediate consequence to changes in the flow conditions at the trailing edge of the airfoil and denoted them as Kutta waves. A widely-cited explanatory model was proposed by Lee [10], and subsequently used to predict the frequency of oscillation [10, 12, 13]. According to the model, two sequential phases of downstream and upstream propagation of disturbances form the recurring buffet cycle. The shock motion initiates pressure waves that subsequently propagate downstream in the separated flow region all the way to the trailing edge. The interaction with the latter emits disturbances that travel upstream along the airfoil surface. These upstream moving Kutta waves are assumed to interact with the shock wave and impart energy [9], allowing to return the shock wave to its original location. That way, the feedback loop is completed, thus ensuring the sustained back and forth motion, i.e. periodic oscillation of the shock wave. Several studies, however, encountered difficulties in reproducing their experimental results with the original formulation of Lee's model. Jacquin et al. [3] and Garnier and Deck [14] report large discrepancies regarding predicted buffet frequencies with deviations of up to 60%. Therefore, refinements and extensions to the model were incited [3, 15, 16] aiming at better agreement with measurements. Giannelis et al. [17] emphasized that these conflicting results indicate a limited robustness of Lee's model to variations in airfoil geometry. Crouch et al. [18] approached the matter from an entirely different perspective, linking the buffet onset with a global instability of the flow. Eigenvalue analyses based on linearized RANS simulations were carried out to determine the stability boundary, and thus incipient shock unsteadiness. This purely mathematical approach contributed to the perception of the phenomenon and enhanced the prediction of buffet onset conditions.

The majority of studies concerned with transonic buffet aim at contributing to a profound understanding of the underlying mechanisms to mitigate buffet and finally prevent the structural response. Substantially less attention has been dedicated to the evolution of the buffet-induced turbulent wake. Regarding the practical implementation in civil aircraft, however, also the influence of the wake on aerodynamic devices downstream of the wing, such as tail plane control surfaces, is crucial, as it may affect their performance.

The formation of wakes downstream of airfoils has been studied for either low-Reynolds number flows [19], non-buffet conditions [20, 21], or mostly laminar flow configurations [22]. Only Szubert et al. [23] addressed fully established shock buffet in turbulent flow at high-Reynolds number and replicated the conditions identified relevant for pronounced buffet by Jacquin et al. [3] in terms of Mach number, angle of attack, and chord-based Reynolds number.

The suction-side-bound oscillatory flow mode of the airfoil and the complex dynamics inherent to the turbulent wake appear to be coupled [22, 23]. A similarly complex interplay between the two domains was also observed for other transonic flows that comprise pronounced vortex streets, e.g. double-wedge profiles with strong separation [24].

For laminar buffet conditions, Zauner and Sandham [22] identified a complex interplay between Kelvin-Helmholtz instabilities in the surface-bound flow towards the rear part of the airfoil, the formation of a von Kármán vortex street aft of the trailing edge, and subsequently shed pressure waves traveling upstream towards to the shock wave. Based on a modal analysis of an established buffet flow using proper orthogonal decomposition, Szubert et al. [23] showed an interaction between the vortex shedding mode and the buffet mode. Events of massive flow separation - not necessarily driven by developed buffet - may thus give rise to von Kármán-like vortex shedding in the vicinity of the trailing edge and beyond in the near wake [23]. Pressure sensors placed along the airfoil upper surface and in the near wake captured strong secondary fluctuations (in addition to the primary buffet oscillation) over a broad range of chordwise stations. These fluctuations were attributed to a von Kármán mode and persisted throughout the entire near-wake domain downstream of the trailing edge [23]. Power spectra of the wall-pressure signals showed the characteristic low-frequency ( $St_c = 0.075$ ) footprint of shock buffet.

For a more global, integral perspective of an entire aircraft, it is necessary to also quantify the dynamics that the buffet phenomenon imposes on the aircraft structure and control surfaces via the wake of the wing or airfoil. The quantitative importance of a) the turbulent wake evolving in fully developed shock buffet mode and b) the relevance of buffet-induced unsteadiness convected downstream on the aerodynamic performance of civil transonic aircraft have

yet to be explored in greater detail. The transition from airfoils to swept wings adds further complexity, including more intricate and partially spanwise-periodic patterns, along with a broadband spectral nature at reduced shock amplitude [2, 25]. To be able to study and understand such effects, mechanisms related to 2D buffet need to be known first. This work aims to contribute to a thorough understanding of 2D configurations. Therefore, we assess the region around the airfoil rear section and the near wake in detail for fully established airfoil buffet conditions, since this buffet mode induces most severe dynamic conditions.

We characterize the temporal and spatial structure of the separated boundary layer and near wake with particular focus on the variation over the buffet cycle. A careful assessment of the wake structure and involved dynamics is the essential groundwork for understanding the complex interaction of a fully established buffet configuration with a tail plane. To the authors' knowledge, this is the first experimental investigation to focus explicitly to the evolution of the buffet-dominated periodic fluctuation of the near wake field by means of optical flow measurement techniques.

In Sect. 2, we introduce the experimental methods and setup, followed by a detailed discussion of the turbulent flow field in Sect. 3. We present our conclusions in Sect. 4.

## 2 Experimental methods and setup

We briefly introduce the experimental facility and investigated airfoil models, before presenting an overview of the applied measurement arrangements. The section is complemented with fundamental considerations of vector field post-processing that form the basis for subsequent sections.

### 2.1 Wind tunnel facility and model

Our experiments were conducted in the Trisonic Wind Tunnel at the Institute of Aerodynamics, RWTH Aachen University. Based on interchangeable test sections and adjustable nozzle geometries, the intermittently-operated vacuum-type indraft facility can provide Mach numbers between  $0.3 < M_\infty < 4.0$ , thus covering subsonic, transonic, as well as supersonic flow conditions. Continuously run screw-type compressors evacuate four vacuum tanks with a total volume of  $380 \text{ m}^3$  downstream of the test section and transport the air through a dryer bed before it enters a large  $180 \text{ m}^3$  air reservoir balloon at ambient conditions. The relative humidity of the air is thus kept below 4 % to preclude condensation effects and falsifications of the measured shock location [26]. A measurement cycle is initialized by the actuation of a fast-acting valve that allows the high and low pressure sections to retrieve equilibrium conditions, thus drafting the measurement medium from the reservoir through the test

section into the vacuum tanks. In each measurement cycle, stable flow conditions are obtained for 2–3 s, depending on the configured Mach number. After each measurement cycle, the same pre-dried air is fed back into the reservoir whereby the closed loop recirculation ensures constantly low relative humidity. Turnaround times of approximately 7 min are achieved. The obtainable Reynolds number is a function of the selected Mach number and the ambient conditions of the resting, pre-dried air in the reservoir. The turbulence intensity based on the freestream velocity fluctuation of the wind tunnel is below 1 %.

For the present study, measurements were conducted at  $M_\infty = 0.72$ , which is equivalent to a free-stream velocity of  $u_\infty = 235 \text{ m/s}$ . For the investigated airfoil, a chord-based Reynolds number of  $Re_c = 2 \cdot 10^6$  is obtained. These conditions require the transonic operation mode. The transonic test section features a rectangular cross section of  $400 \text{ mm} \times 400 \text{ mm}$  and a total length of 1410 mm.

It is equipped with flexible upper and lower walls to compensate the influence of solid walls confining the flow and to emulate conditions in terms of streamline contouring observed in the equivalent free, unconfined flow around the same airfoil geometry [27].

We studied buffet on the supercritical OAT15A airfoil. The two-dimensional wind tunnel model has a relative thickness of 12.3 % and features a total span of 399 mm, which is equivalent to the width of the test section. A chord length of  $c = 150 \text{ mm}$  was chosen, giving an aspect ratio of approx. 2.66. The upper and lower half of the model were manufactured from stainless steel, along with a trailing edge made of metal particle-filled epoxy resin. The center of rotation for the angle of attack is located at about mid-chord of the airfoil. As earlier buffet studies suggest a non-negligible implication on the buffet boundary [28, 29], the structural properties of the applied model were assessed across various operating conditions, i.e. aerodynamic load settings. Optical flow measurements used to track the surface motion in time revealed that even under most severe buffet conditions, no substantial model deformation was detected. Fig. 1 shows a schematic representation of the airfoil installed in the optically accessible test section.

### 2.2 Measurement arrangement

Flow visualizations are obtained with a focusing schlieren setup, where extended grids illuminated by correspondingly large illuminated surfaces replace the point-shaped light sources used in classical schlieren arrangements [30, 31]. A focusing schlieren system inspired by Weinstein's approach [32] has been developed by the authors [33] to explore flow configurations in the transonic and supersonic flow regime.

This system overcomes some of the limitations of classical schlieren configurations, in particular the close to infinite

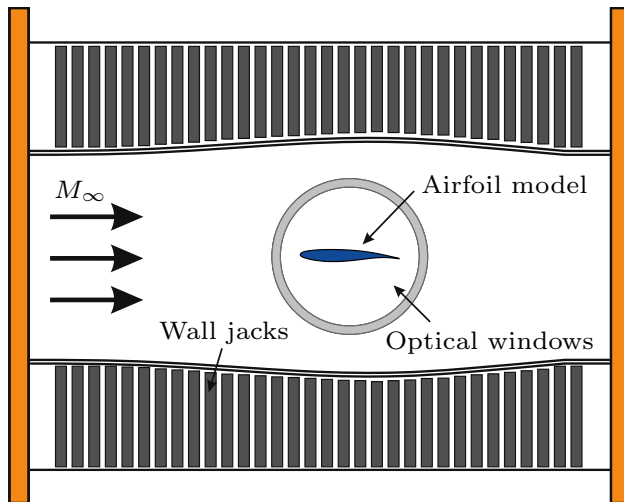
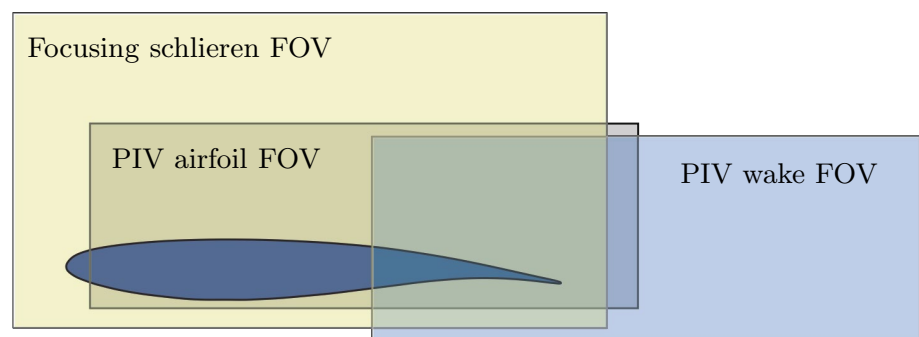


**Fig. 1** Illustration of the transonic test section with adjustable walls

depth of focus that results in strong line-of-sight integration. We require the ability to focus on narrow slices of the flow to be able to analyze our highly unsteady and partially three-dimensional flow of interest.

The flow was illuminated by a  $3 \times 3$  array of 15 W high-power LEDs together with a constant-current source with an electric output adjustable between 50 W and 120 W. The source grid consists of CNC-machined alternating clear and opaque lines, the cutoff grid is an exact photographic negative of the source grid. A large 470 mm Fresnel lens, placed slightly ahead of the source grid, captures major portions of the light intensity, illuminates the source grid evenly bright by reshaping the light cone, and redirects the light beam through the test section past the model and onto the schlieren lens. The illuminated measurement area around the spanwise centerplane of the airfoil has a diameter of 280 mm. However, the outer edges are subject to vignetting due to the light beam passing through two consecutive circular windows. An effective field of view (FOV) without vignetting of  $d_{FS} \approx 220$  mm was achieved, using a magnification  $M_{FS}$  of 0.2 between the two grids in conjunction with the relay optics and a 35 mm camera lens.

**Fig. 2** Schematic overview of the different covered camera fields of view captured by the PIV and focusing schlieren setups; all systems are aligned with the model center plane



To temporally resolve the oscillatory motion of the shock, the schlieren visualizations were recorded with a Photron SA-5 CMOS high-speed camera at a frame rate of 20 kHz and with a short exposure of  $1.9 \mu\text{s}$ . For the high-speed recording, a FOV of 180 mm width and 130 mm height is projected on the camera sensor, yielding an effective resolution of 4.05 px/mm.

The focusing schlieren setup was operated with a horizontally aligned cutoff grid to capture vertical density gradients. From these measurements, we extracted the temporal development of the SWBLI and the near wake, the shock position and amplitude, as well as the shock oscillation frequencies.

To acquire detailed velocity data, we applied particle image velocimetry (PIV). Planar measurements are performed in a streamwise/wall-normal plane along the centerline of the airfoil model (Fig. 2).

A Litron Nano PIV double pulsed Nd:YLF laser, operating at a wavelength of 527 nm, produces a light sheet of 1.5 mm thickness. The large laser-pulse energy of 200 mJ/pulse with a pulse duration of 4 ns ensures a high signal-to-noise ratio. The flow is seeded with di-ethyl-hexyl-sebacate (DEHS) tracer droplets with a mean diameter of  $1 \mu\text{m}$ . Particle images are captured using two identical FlowSense EO 11M CCD cameras with a resolution of 11 megapixels, which corresponds to a sensor resolution of 4,008 pixels  $\times$  2,672 pixels at a pixel size of  $9 \mu\text{m}$ . Both cameras are focused on the same FOV to increase the acquisition rate to 10 Hz. The FOV covers both the vicinity of the airfoil trailing edge and the near wake. It is 145 mm wide and 80 mm high, thus spanning a streamwise domain from 0.6 to 1.7 c. Based on the magnification of  $1/4.04$ , a spatial resolution of  $27.56 \text{ px m}^{-1}\text{m}$  is obtained. With a final interrogation-window size of  $16 \text{ px} \times 16 \text{ px}$  at an overlap of 50 %, the resulting velocity maps feature a vector spacing of 0.29 mm. Relevant parameters of the focusing schlieren and PIV tests are summarized in Table 1.

### 2.3 Identification of buffet phases

Preceding analyses of the buffet flow around the OAT15A airfoil (see [34]) with a field of view covering the entire



**Table 1** Overview of experimental PIV and FS parameters

| Particle image velocimetry setup |             |         | Focusing Schlieren setup |           |         |
|----------------------------------|-------------|---------|--------------------------|-----------|---------|
| Sensor resolution                | 4008 × 2672 | px × px | Sensor resolution        | 704 × 520 | px × px |
| FOV width                        | 150         | mm      | FOV width                | 180       | mm      |
| FOV height                       | 80          | mm      | FOV height               | 150       | mm      |
| Acquisition rate                 | 10          | Hz      | Acquisition rate         | 20,000    | Hz      |
| Temporal separation              | 4           | μs      | Shutter speed            | 1/525,000 | s       |
| Spatial resolution               | 27.56       | px/mm   | Spatial resolution       | 4.05      | px/mm   |

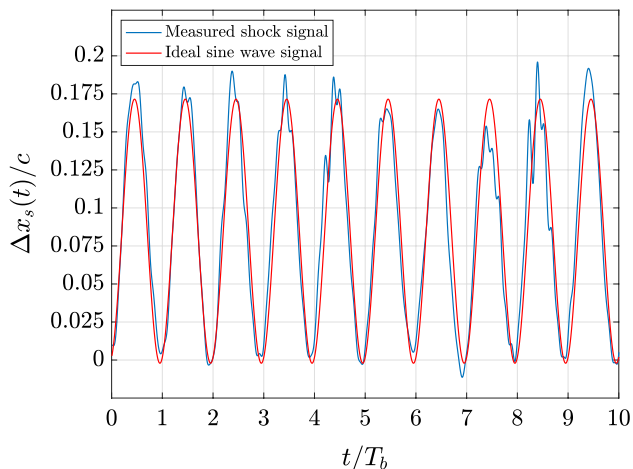


**Fig. 3** Extracted time signal of shock motion for  $M_\infty = 0.72$  and  $\alpha = 5.0^\circ$  and superimposed sinusoidal signal, evaluated for 10 complete buffet cycles

suction side from 0.1 to 1.1 c. revealed large-scale global modifications of the flow topology throughout the buffet cycle. High-speed focusing schlieren sequences were evaluated to track the shock oscillation in time. Fig. 3 captures the shock motion along the airfoil chord over 10 buffet periods.

On the basis of the history of the shock motion displayed in Fig. 3, we assume a quasi-periodic behavior of the buffet motion. In addition, the shock motion covers almost 20 % of the chord and is coupled with intermittent flow separation and reattachment (see also Fig. 4). Therefore, statistics for discrete phases of the buffet cycle are more meaningful than a global mean and a phase-related consideration of the phenomenon is justified.

Therefore, we thoroughly aligned the knowledge gathered from focusing schlieren measurements with the observations from PIV, and demonstrated that individual buffet phases can be unambiguously assessed based on the instantaneous shock location, the shape of the shock front, and the shock inclination near the airfoil contour for each uncorrelated snapshot [34], which then forms the basis of phase assignment. An overview of the thus obtained phases is given in Fig. 4.

In particular, we consider the most upstream location of the shock, which corresponds to the conditions of most pronounced wake (Fig. 4a); the shock’s incipient downstream movement (Fig. 4b); the approximate mean shock location as intermittent chordwise position during the downstream phase (Fig. 4c); the final phase of shock downstream progression (Fig. 4d); the most downstream shock location (Fig. 4e); the state of incipient upstream excursion (Fig. 4f); the approximate mean shock location occupied during the upstream movement (Fig. 4g); and the final phase of upstream movement close to the reversal point (Fig. 4h).

Based on a sufficiently large overlap between the fields of view in the present and the earlier [34] measurement campaign, we were able to apply a congruent phase-average approach and transfer the relevant quantities to the rear portion of the airfoil and the near wake, yet excluding the actual shock wave. The procedure and evaluated parameters are clarified in Fig. 5.

First, the integral velocity magnitude within the rectangular analysis window in Fig. 5 (4) is evaluated in terms of the percentage of vectors that exceed or stay below a certain threshold ( $u \leq 0.25 u_\infty$ ). Threshold values were previously identified to uniquely describe the chordwise location of the shock and thus allow the definition of characteristic phases within the buffet cycle. This procedure allows to pre-assign the snapshots to the respective buffet phases. This criterion was complemented by considering the height of the low-momentum bubble (see Fig. 5 (5)). However, due to similar velocity defects for phases of final upstream motion and incipient downstream motion, some ambiguity remains in this first classification.

Second, the streamwise velocity magnitude at three chordwise stations (location (1), (2), and (3); Fig. 5) were compared with reference values from the predefined phase assignment (see Fig. 4) for each snapshot.

An analysis of the thus finally obtained phase assignment in the field of view covering the entire airfoil suction side (studied in [34]) revealed that each buffet phase induces characteristic velocity defects. These deficits are modulated by the direction of motion and strength of the shock wave. This third criterion is independent of the velocity deficit in the strongly separated region and can eliminate the last ambiguity in the phase assignment.

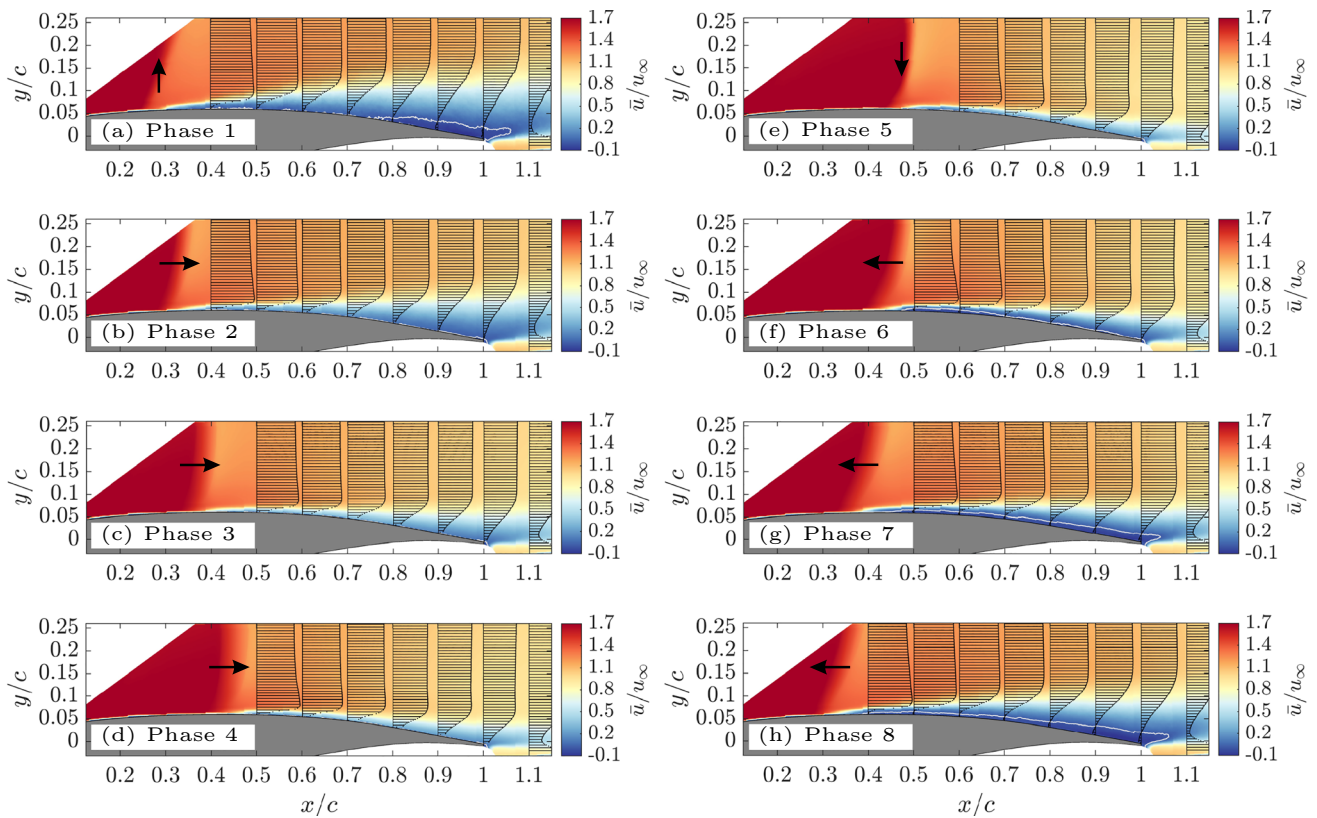
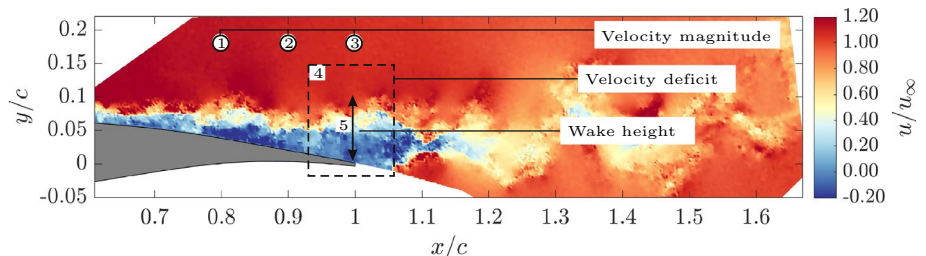


**Fig. 4** Phase-averaged streamwise velocity maps and profiles for characteristic phases of the buffet cycle. Arrows indicate the associated direction of shock motion (arrow up: upstream reversal point;

arrow down: downstream reversal point). Gray isolines  $\bar{u}/u_\infty = 0$  denote regions of reverse flow

**Fig. 5** Overview of criteria used for buffet phase assignment for instantaneous velocity fields in the wake



Finally, as a consistency check, the velocity profiles at the chordwise stations between  $x/c = 0.8$  to  $x/c = 1.1$  of the present case and the case studied in [34] were examined for congruence. The results showed excellent agreement (less than 0.6% deviation), which proves that we can successfully identify the respective buffet phase of a snapshot without directly knowing the shock position. The respective number of flow fields used for the subsequent statistical analysis are as follows: 203 snapshots for phase 1, 271 snapshots for phase 2, 589 snapshots for phase 3, 644 snapshots for phase 4, 511 snapshots for phase 5, 369 snapshots for phase 6, 408 snapshots for phase 7, and 204 snapshots for phase 8.

### 3 Results and discussion

Since the flow varies considerably throughout a buffet cycle, and these variations have a strong impact on the wake of the airfoil, we begin this section with a short discussion of the flow topology on the airfoil suction side for fully established buffet conditions. We then briefly discuss the rear section of the airfoil and near-wake region ( $0.6 \leq x/c \leq 1.7$ ) on the basis of ensemble-averaged velocity maps. Subsequently, we discuss the wake structure in detail, using phase-distinguished representations of instantaneous and averaged velocity fields in the streamwise and

vertical directions. We also provide a discussion of turbulent quantities and the vorticity, as well as a spectral analysis of the vortex shedding at the trailing edge.

### 3.1 Shock-buffet induced variation of the flow topology

We briefly summarize the strongly varying flow topology, since it lays the basis for the subsequent analysis of the wake properties. An in-depth discussion of the data has been provided in [34] and [35].

An overview of selected phases of the buffet cycle is given in Fig. 6, which shows the huge periodic variation of the flow, which coincides with a back and forth motion of the shock wave that covers approx. 20% of the airfoil chord. The instantaneous flow fields indicate a strongly turbulent wake with numerous turbulent eddies of varying size. To account for, and quantify, the large-scale variation of the global flow topology, we analyzed the velocity fields from PIV in a phased-averaged manner according to the phases discussed in the previous paragraph and following the procedure outlined in Sect. 2.3. Fig. 4 shows the resulting phase-averaged streamwise velocity contours. Arrows indicate the respective direction of motion of the shock wave associated with each phase.

The first phase (Figs. 4a and 6a) corresponds to the most upstream shock location close to the reversal point, for which the separated boundary layer thickens strongly and the wake is of large surface-normal extent. The severity of flow separation is further substantiated in the great velocity deficit in the near-wake velocity profile at  $x/c = 1.1$  (Fig. 4a).

Phase 2 denotes the phase of incipient downstream motion of the shock wave, which is accompanied by a successive reduction in separation. Compared with phase 1, the shock line is less oblique, and has moved from  $x/c \approx 0.23$  to  $x/c \approx 0.28$  (see Figs. 4b and 6b).

The observed trends continue in phase 3 (Fig. 4c), in which the vertical extent of the wake and its related momentum deficit have reduced by almost 75% compared with phase 1. The continued downstream motion of the shock wave causes an ongoing straightening of the shock [34, 35], which becomes more evident in Fig. 6c.

The continued downstream displacement of the shock wave from  $0.35c$  to  $0.40c$  between phases 3 and 4 is accompanied by a further contraction of the turbulent wake, most apparent in fuller velocity profiles close to the wall (Figs. 4d and 6d).

Phase 5 (see Figs. 4e and Fig. 6e) denotes the most downstream shock location ( $x/c \approx 0.48$ ). The shock line is now exactly normal, and the  $\lambda$ -region has reached its minimal extent. The flow is completely attached all along the suction side, and the wake influence is only noticeable in the immediate vicinity of the airfoil contour.

At the onset of the shock's upstream motion captured in phases 6 and 7 (Fig. 4f and g), the shock starts to tilt back and the separation region increases. The maximum upstream shock velocity is not yet reached. Both the wake size and velocity deficit close to the wall are greater than in the corresponding shock location in phases 3 and 4 during the shock downstream motion. The velocity profiles of phase 7 are significantly less full than for phase 5, and the wake increases. The  $\bar{u}$  velocities thus contain negative values all the way until the TE (compare the isoline in Fig. 4g). The distinct obliqueness of the shock line and the large  $\lambda$ -structure are both finely reproduced in the schlieren data (see Fig. 6f and g).

The final phase of the shock upstream motion is represented by phase 8 (Fig. 4h and Fig. 6h), in which the low-momentum wake protrudes even farther into the outer flow than in the previous phase, and the induced momentum deficit is significantly more severe. The deficit even results in a small region of reverse flow close to the airfoil surface with a vertical extent of  $y/c \approx 0.025$  above the trailing edge,

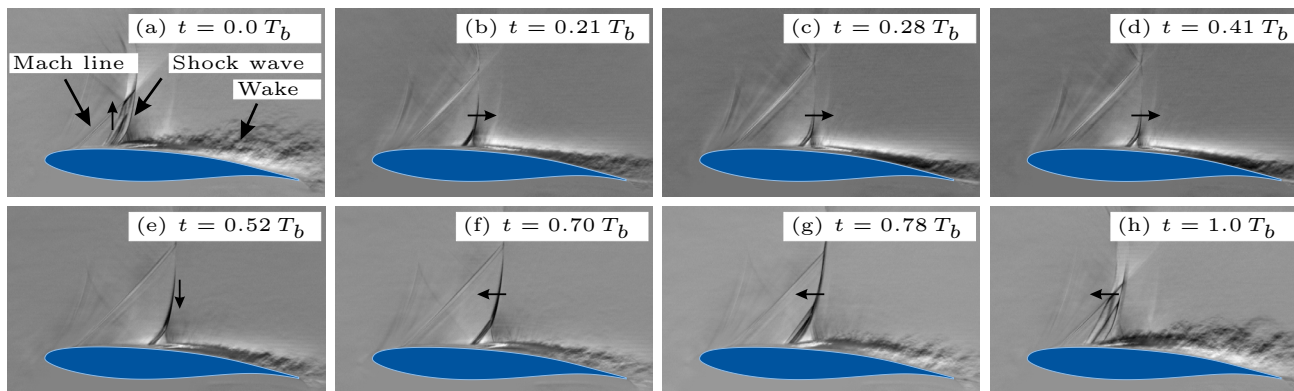


**Fig. 6** Focusing schlieren snapshots capturing the global variation of the flow topology over the full buffet cycle  $T_b$ . Arrows indicate the current direction of shock motion (arrow up: upstream reversal point; arrow down: downstream reversal point)

comparable to phase 1 (Fig. 4a). Table 2 summarizes the phase assignment criteria and processed snapshot quantities.

The flapping behavior of the turbulent wake shown in Fig. 6 is now assessed in a more quantitative manner. The turbulent wake varies strongly throughout the buffet cycle, whereby its extent is coupled with the direction of shock motion. Since the shock motion is periodic, we expected a phase coupling of the wake size with the shock position. To verify this assumption, we estimated the relative size of the turbulent shear layer and wake along the chord length throughout the buffet cycle. A gradient-based detection was applied to the time-resolved schlieren sequences to extract the respective boundaries of the shear layer, here demarcated by a sharp transition between areas of strong gradients, i.e. pixel intensity fluctuations, and a homogeneous background. Then, the area enclosed by these edges was calculated and used as an estimate of the turbulent wake area  $A_w$ . Overall, we evaluated 60 complete buffet cycles, i.e. over 10,000 images. The time history of the shock position  $x_s$  (in relation to the chord length) and separated wake area (normalized with its temporal mean extent  $\bar{A}_w$ ) are shown in Fig. 7.

As evident in the time plot, the quantities indicate phase-locked modulation of the shock and separated boundary layer, i.e. the shear layer thickens as the shock wave advances upstream and thins during shock's downstream progression. The latter observation is qualitatively consistent with findings reported in [1] and [36]. These quantities thus oscillate at an identical frequency, however, at an almost constant, finite phase shift. Performing a cross-correlation of the two signals yields a wake area preceding the shock

motion by approximately 0.3491 rad at its most upstream, and by 0.5585 rad at its most downstream location. The wake size reaches its minimum extent shortly before the shock occupies its most downstream location. The wake size already begins to increase before the shock passes its reversal point, and reaches its maximum towards the final phase of the shock upstream movement. Overall, comparing its most extreme conditions, the wake area grows by a factor of 2.5 within a full buffet cycle, and performs a pronounced, recurrent flapping motion.

### 3.2 Mean velocity maps in the near wake

Before discussing the strong periodic variation of the wake flow field, we present ensemble-averaged velocity maps of the streamwise and vertical velocity components in Figs. 8 and 9, respectively. This global representation approximates the temporally-averaged flow physics and allows to assess and quantify the impact of the buffet state on aerodynamic components located downstream of the wing along the wake from an integral perspective.

Both  $u/u_\infty = 0.05$  (dashed line) and  $u/u_\infty = 0.1$  (solid line) isolines are superimposed with the mean streamwise velocity contour map in Fig. 8 to illustrate the substantial momentum loss on the basis of an ensemble averaged flow field. Recalling the phase-averaged discussion in Fig. 4, we notice that the  $u/u_\infty = 0.1$  isoline encloses a low-momentum domain that resembles the velocity field attributed to phases 4 and 6. In view of the fully recovered condition evidenced for phase 5, we infer that a significant amount of intermittently very low momentum flow near the trailing edge must contribute to this global mean.

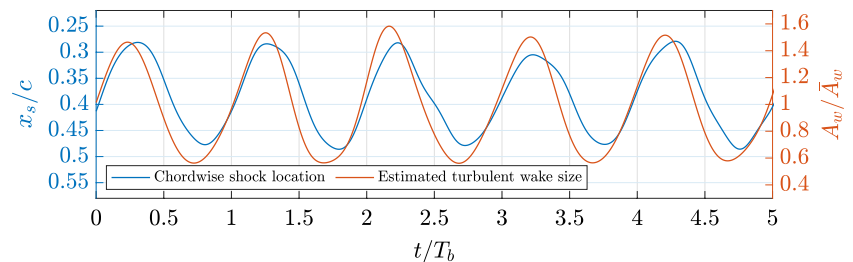
As will be shown later in the context of Fig. 16, this region is a result of the vigorous shock dynamics, in particular phases of upstream shock motion, for which reverse flow extends over large parts of the rear of the airfoil up until the trailing edge. The greatest velocity deficit occurs close to the surface and in the inner wake core region (visible as blue streak with  $u \leq 0.25 u_\infty$  in Fig. 8). The low-momentum deficit increases with downstream development. Furthermore, the wake center shifts slightly upwards.

The vertical velocity map is structured into three characteristic subdomains (see Fig. 9): a pronounced downwash

**Table 2** Overview of buffet phase assignment

|         | Phase angle | Phase width | Snapshots |
|---------|-------------|-------------|-----------|
| Phase 1 | 0.7854 rad  | 0.00836 c   | 234       |
| Phase 2 | 0.7854 rad  | 0.05951 c   | 476       |
| Phase 3 | 0.7854 rad  | 0.0842 c    | 1433      |
| Phase 4 | 0.7854 rad  | 0.05951 c   | 1437      |
| Phase 5 | 0.7854 rad  | 0.00836     | 254       |
| Phase 6 | 0.7854 rad  | 0.05951 c   | 637       |
| Phase 7 | 0.7854 rad  | 0.0842 c    | 675       |
| Phase 8 | 0.7854 rad  | 0.05951 c   | 604       |

**Fig. 7** Temporal development of upstream and downstream shock motion (in blue) in comparison with the evolution of the highly turbulent wake region (in red)





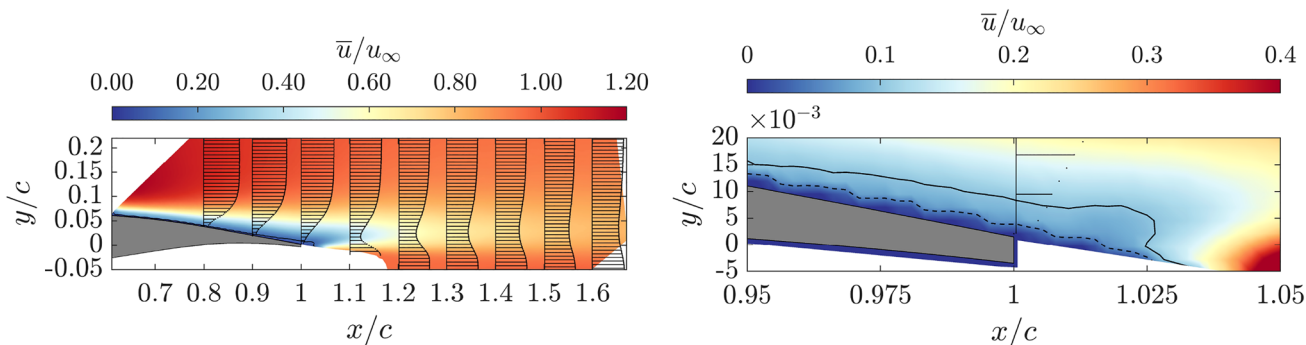


**Fig. 8** Ensemble-averaged streamwise velocity map and profiles at characteristic chordwise locations in the near wake for fully established buffet at  $M = 0.72$  and  $AoA = 5$  deg. Isolines indicate regions where  $\bar{u}/u_\infty = 0.05$  (dashed line) and  $\bar{u}/u_\infty = 0.1$  (solid line)

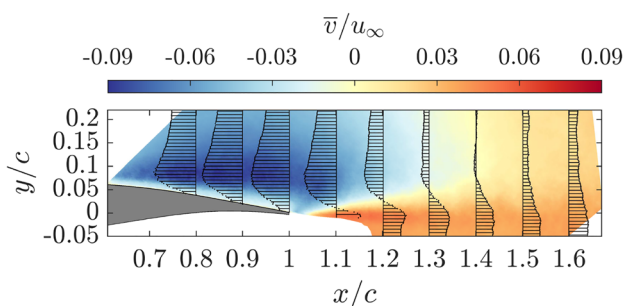


**Fig. 9** Ensemble-averaged vertical velocity map and profiles at characteristic chordwise locations in the near wake for fully established buffet at  $M = 0.72$  and  $AoA = 5$  deg

region along the aft section of the airfoil, an upwash region downstream of the trailing edge, which emanates from the pressure side, and a region of almost vanishing  $v$ -component further downstream of the airfoil in the upper half of the wake. These regions are captured by the velocity profiles at chordwise stations  $x/c = 1.1$  to  $x/c = 1.4$ . At  $0.1c$  aft of the trailing edge, a sharp distinction between up- and downwash is dominant. The upwash from the pressure side seems to gradually overcompensate the downwash component, yielding a close-to-zero vertical flow component in the upper half of the captured domain at  $x/c = 1.4$ . In view of the scenario outlined above, assuming a strongly perturbed wake impinges on a tail plane located farther downstream, we derive the following scenario: the prolonged wake domain at chordwise stations  $x/c = 1.5$  and  $x/c = 1.6$  indicates that the pressure-side-dominated upwash gradually overcompensates the downwash component, resulting in a uniformly positive  $\bar{v}$  from  $x/c = 1.5$ . The average vertical velocity component evaluated along the vertical sections at  $x/c = 1.5$  and  $x/c = 1.6$  is  $4.9$  m/s and  $5.8$  m/s, respectively. With the mean horizontal velocity components of  $206$  m/s and  $210$  m/s, respectively, evaluated at the same chordwise stations, flow angles of  $1.36$  deg and  $1.58$  deg are obtained, which indicate

a positive (upwash) component with respect to the airfoil chord. However, taking into account the positive  $AoA$  of  $5$  deg in the present experiment, the buffet-induced wake still causes an effective downwash with reference to the direction of the incoming flow. Obvious implications on a potential HTP flow are a reduced effective  $AoA$  and thus an off-design mode of operation.

### 3.3 Instantaneous modification of the wake velocity field by buffet

Despite the considerable level of turbulent perturbations in instantaneous flow representations, they convey important features characterizing the nature of the dynamic flow field that are precluded in phase- or ensemble-averaged velocity contours. These features include turbulent structures, shedding of vortices, and the overall extent of the turbulent wake.

The instantaneous vertical velocity contours show a turbulent wake of large extent in all phases of far upstream shock locations, namely phases 1, 2, 7, and 8 (see Fig. 11b, d, n, p). In comparison, the flow topology gradually recovers when the shock progresses towards its most downstream location (phases 3, 4, and 5 in Fig. 11e, h, and k. Turbulent structures are confined to a narrow band, as most clearly visible in phase 5 (Fig. 11j).

The phase overview reveals that wider wakes (e.g. phase 1 and 8) are associated with low-frequency/high-wavelength vortex shedding and increased turbulent intensity, whereas narrower wakes coincide with high-frequency/low wavelength vortex shedding behavior.

Another characteristic pattern nicely captured in the streamwise velocity maps (left column of Fig. 11) is the slip line emanating from the triple-point location of the lambda shock structure. This feature is most clearly reproduced in phases 4, 5, and 6 (Fig. 11g, i, and k), i.e. when the separation regions are smaller. The large separation in the remaining phases widens the lambda structure and pushes the triple point upwards. For a better understanding, both the triple



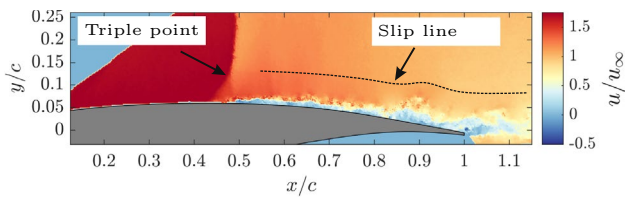


**Fig. 10** Instantaneous streamwise velocity maps showing upstream field of view, including lambda shock structure and slip line originating from the triple point

point and the slip line are plotted for the suction side FOV in Fig. 10. The corresponding continued slip line is depicted in Fig. 11 (i) for the downstream FOV (note that the slip line is enhanced by a dashed line in both figures, due to the relative weakness of that feature).

Phases of pronounced momentum deficit and large-scale separation (phases 1, 2, 7, and 8) show concomitant intense perturbations in the vertical velocity component. These manifest themselves in a regular pattern of alternating velocity regions of opposite sign, forming interlaced structures with

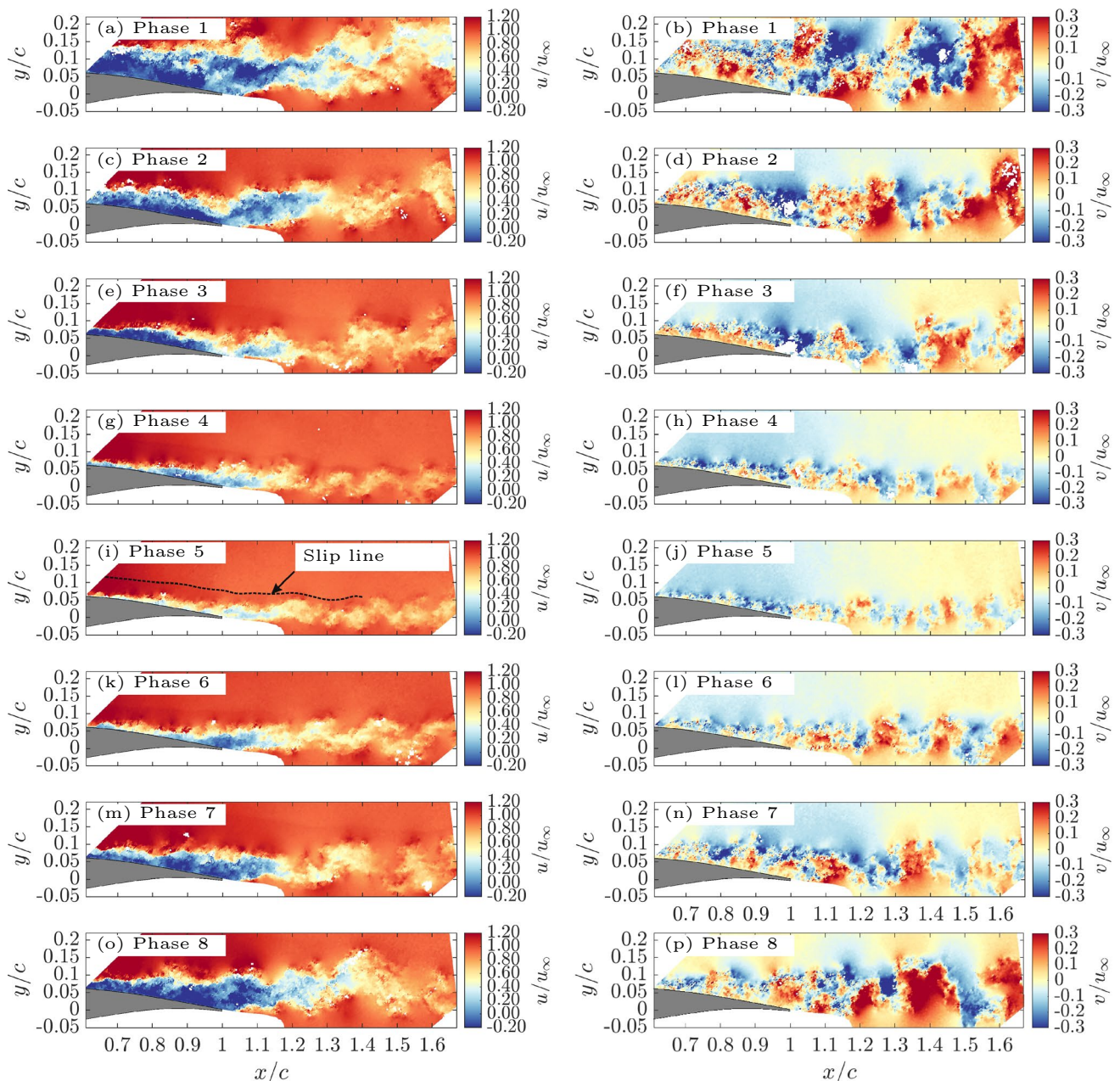


**Fig. 11** Instantaneous streamwise (left column) and vertical (right column) velocity maps for characteristic phases of the buffet cycle

positive (upwards) contributions from the pressure side and negative (downwards) contributions from the suction side.

The size and intensity of these velocity perturbations vary considerably in sync with the buffet cycle. Coherent patches of positive or negative fluctuations in the vertical velocity component are largest when the shock is far upstream, and shrink with downstream shock displacement. The fluctuation magnitude of  $\pm 0.25u_\infty$  remains almost constant between  $x/c = 1.0$  and  $x/c = 1.7$ , which suggests a relevant influence of this phenomenon even farther downstream.

To complement the findings inherent to the velocity fluctuations (Fig. 11), we compute the vorticity field on the basis of the streamwise and vertical components of instantaneous velocity maps according to Eq. 1. As this quantity is invariant to coordinate transformation, it allows to robustly track the vorticity produced in the boundary layer as it gets diffused in the vertical direction and convected downstream in the wake.

$$\omega_z = \frac{\partial v}{\partial x} - \frac{\partial u}{\partial y} \tag{1}$$

Not only the intermittently strongly separated flow field in transonic buffet conditions is associated with the formation of vortex streets [22], focusing schlieren sequences furthermore indicated vortices shed from the trailing edge and convected downstream. By exploring the vorticity distribution across different buffet phases, we hope to assess buffet-induced disturbances more easily and resolve the

vortex-shedding process captured by coherent pockets of vorticity.

Figure 12 displays the instantaneous vorticity distribution pertaining to the characteristic phases of the buffet period introduced above: starting from the most upstream shock location (a), to its most downstream shock position in phase 5 (e), to the final phase of upstream motion in phase 8 (h). We observe the convection of vorticity in the near wake and throughout the vortex shedding process at the trailing edge, as well as the strong variation of the involved regions with intense vorticity coupled with the buffet phase. The slip line originating from the triple point of the lambda shock structure is well-resolved by the in-plane vorticity maps derived from PIV: it is visible as a thin streak of moderately positive vorticity that follows the vertical extent of the wake and is almost parallel to the edges of the turbulent wake (see e.g. Fig. 12e).

The vorticity representation also confirms and clarifies the observed vortex roll-up mechanism identified in Fig. 11. We discern coherent, alternating vortical structures that are convected downstream of the trailing edge across all phases of the buffet cycle. Their size and spatial distribution within a buffet period shows a cyclic variation, which confirms the expected intermittent change between low-frequency/high-wavelength and high-frequency/low wavelength behavior. The contribution from the lower half of the wake is consistently positive, and negative vorticity is shed along the upper half. This tendency was previously observed by Szubert

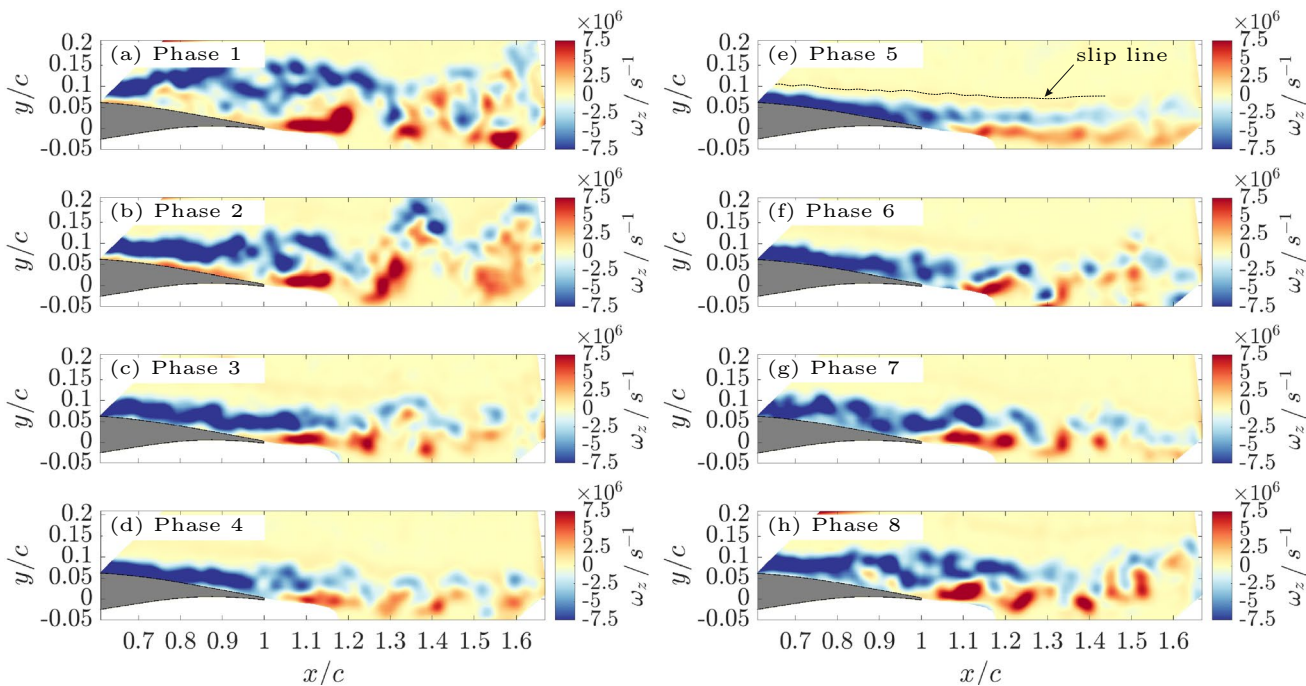


Fig. 12 Representative instantaneous vorticity contour maps for characteristic phases of the buffet cycle

et al. [23] based on consecutive snapshots covering one vortex shedding period.

As discussed above, buffet phase 1 captures the most upstream shock locations and is associated with massive flow separation with a vertical extent of the turbulent wake of almost  $0.2c$ . The corresponding vorticity map in Fig. 12a reveals two aspects of its macroscopic organization: first, Kelvin-Helmholtz-type instabilities develop downstream of the shock wave up to about  $x/c = 1.2$ ; second, a pronounced vortex roll-up is observed around the trailing edge and behind.

Considering Fig. 12, and taking into account the vorticity maps provided by Szubert et al. [23], we observe qualitative agreement in terms of vorticity spacing and distribution along the main trajectory of the turbulent wake, in particular in phases with an upstream traveling shock wave inducing the formation of a large wake (see Fig. 14a and h).

Attempting to quantify the vortex shedding mechanism, Szubert et al. provide a characteristic time scale of the vortex shedding period of 0.38 ms, from which a corresponding shedding frequency of 2630 Hz can be derived. We used high-speed focusing schlieren sequences to visually track the shedding and convection of the vortical structures. Due to the downstream limit of the camera field of view, however, tracking of individual vortices was challenging and only possible over 6–8 consecutive frames. Nonetheless, as the time step between two successive coherent structures was 3–5 frames on average, an estimate of the shedding frequency could be determined. Only comparing phases of strong flow separation and large wake, a characteristic time scale of 0.29 ms was found. This is on the same order as reported by [23], and corresponds to a frequency of 3400 Hz. Further taking into account the smaller buffet frequency of 78.1 Hz in [23] compared to this experiment (113 Hz) while matching Strouhal numbers, a corrected shedding frequency of 2350 Hz can be estimated for the present case. This corrected frequency allows for a more reasonable comparison of the two studies and confirms decent agreement. Similar behavior in both studies is further detected in the downstream evolution of these structures. The vorticity magnitude is decaying substantially only beyond  $x/c = 1.5$  in the numerical work. In our experiment, we also observe maximum values up to approximately  $x/c = 1.5$ , farther downstream smeared out vorticity streaks at decreasing strength prevail.

The quantitative differences between buffet phases are quite severe. In contrast to the widely separated shear layer and large coherent vortical structures in the wake of phase 1, phase 5 exhibits small-scale vortical structures confined to a narrow band. The vortical structures are organized along a more stratified pattern and protrude less far into the vertical direction. Moreover, structures of opposite sign appear less entangled with each other. Overall, this results in an almost sharp separation between positive contributions from the

lower side of the wake and negative contributions from the upper side (compare Fig. 12a and b). This observation is in good agreement with the findings of Epstein et al. [20], that an unseparated transonic flow past an airfoil exhibits considerably reduced vortex shedding.

The massive thickening of the boundary layer in the aft section of the airfoil results in a pronounced de-cambering effect. Hence, the periodic variation between fully-separated and mostly reattached flow throughout a buffet cycle results in a continuous alteration of the integral circulation around the airfoil and therefore in continuous shedding of vorticity aft of the trailing edge. This effect presumably also contributes to the strongly alternating vortex shedding intensity.

Szubert et al. [23] pointed out that events of massive flow separation—not necessarily driven by transonic buffet—may induce von Kármán-like vortex shedding in the vicinity of the trailing edge and the near wake. With pressure sensors placed along the airfoil upper surface and in the near wake, they captured strong secondary fluctuations (in addition to the primary buffet oscillation) over a broad range of chordwise stations. These fluctuations—attributed to a von Kármán mode—reach their maximum at  $x/c = 1.2$ , remain pronounced until  $x/c = 1.5$ , and only decay beyond one chord length downstream of the trailing edge [23]. In the wall-pressure spectra, Szubert et al. [23] observed distinct contributions at higher frequency ( $St_c = 2.5$ ) close to the trailing edge in addition to the characteristic low-frequency ( $St_c = 0.075$ ) footprint of shock buffet. Szubert et al. [23] verified the relation of the  $St_c = 2.5$  peak with the vortex shedding event on the basis of series of instantaneous vorticity maps with adequate temporal resolution.

Operating our focusing schlieren setup with a vertically-oriented grid gives access to the governing horizontal density variations. This way, we explore vortical structures and attempt to draw conclusions on the manner in which they are shed from the trailing edge. The vortex cores of the von Kármán vortex street induced upon the interaction of the flow with the trailing edge are resolved by alternating dark and bright spots in the schlieren visualizations shown in Fig. 13.

High-speed sequences were evaluated using suitable sensor locations, thus allowing us to track the transition of vortical structures, usually encountered as a time history of an alternating dark/bright boundary. As visible in the detail views at the trailing edge (lower row of Fig. 13), both the distinctness and spatial extent of the resolved vortex cores decrease from phases 1–5, i.e. in the course of shock downstream progression (Fig. 13a–c). Assuming that the density gradient scales with the vortex strength, the strength decreases with increasing chordwise shock location. This observation is in good agreement with the shrinking of the vortex street (see Fig. 12). We then perform a spectral density estimation using Welch's method [37] on the obtained



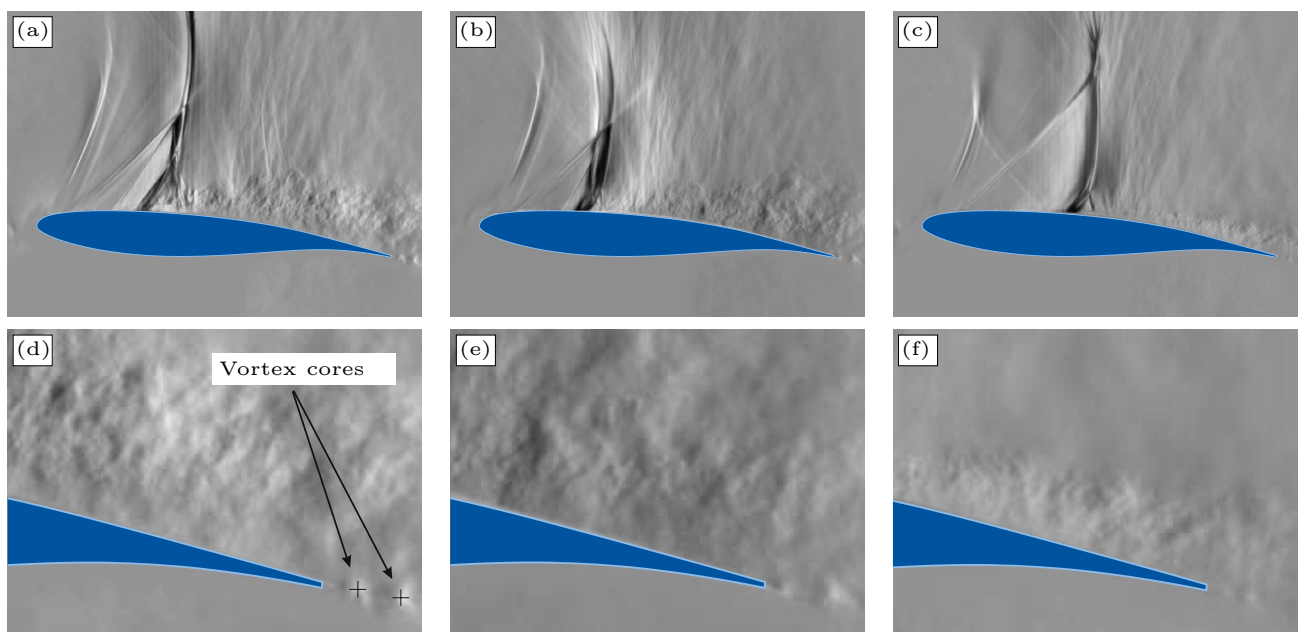


**Fig. 13** Schlieren visualizations of the vortex shedding downstream of the trailing edge for different shock locations: **a** most upstream, **b** incipient downstream motion, and **c** most downstream shock position.

Second row: zooms of the trailing-edge region (**d–f**); vortex shedding indicated with arrows. Sensor locations are marked with crosses

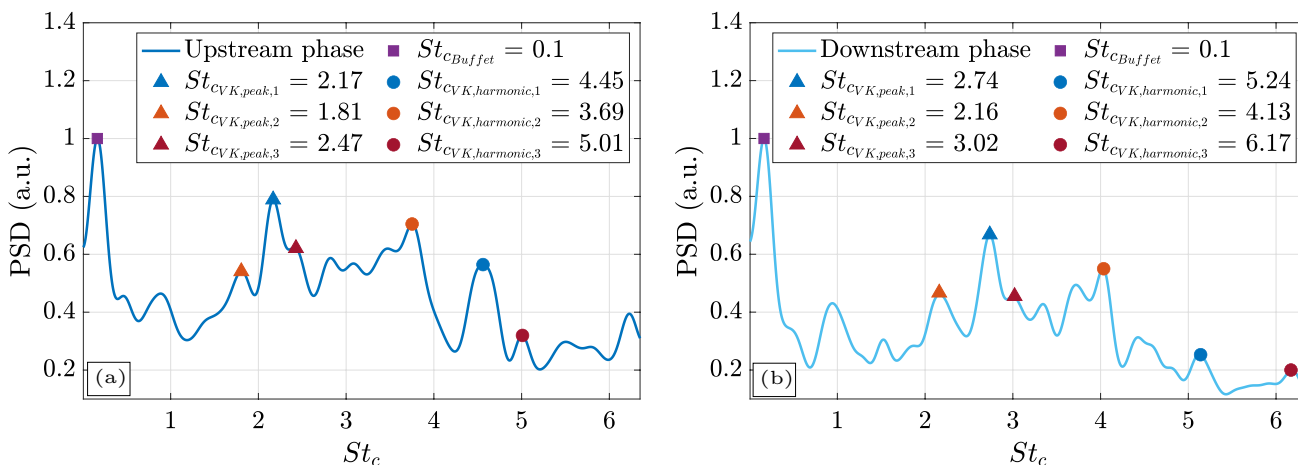


**Fig. 14** Power spectral density distribution of the von Kármán vortex shedding at the trailing edge, according to shock upstream motion (**a**) and shock downstream motion (**b**)

time vector, which in turn is used to analyze the spectral content of the vortex shedding quantitatively. We expect an influence of the observed vortex shedding behavior (elucidated in detail in the context of Figs. 11 and 12) also in the spectra. Preliminary analyses confirmed the assumption, i.e. showing several spikes between  $St_c = 2$  and  $St_c = 3$ , thus forming a broadband bump spanning that same range. This feature, however, inhibits the unambiguous identification of conditional effects, in particular the separation of influences related to the upstream and downstream shock

motions. Therefore, we first fragmented the original time signal into half-cycle sequences, dividing shock upstream and downstream motions. Subsequently, the segments were recomposed into two pseudo time signals, based on which we conducted a similar analysis as presented by Szubert et al. [23]. This approach yields two separate Welch spectra for the shock upstream and downstream motion (see Fig. 14a and b, respectively).

The global buffet mode dominates the flow and affects large parts of the flow domain. Therefore, amongst other

phenomena, the low-frequency flapping motion of the separated shear layer (dominant low-frequency buffet peak at  $St_c = 0.071$ ) is equally visible in both spectra. Another phase-independent element is the moderate spike around  $St_c = 1$  related to the pulsed operation of the LED light source.

Otherwise, both plots exhibit a characteristic footprint with three relevant contributions in the expected  $St_c$  range. The presumed vortex shedding mechanism is associated with Strouhal numbers between 1.81 and 2.47, centered around  $St_c = 2.17$  (see also Fig. 14a).

These findings agree well with the results of Szubert et al. [23], who report a spectral bump at  $St_c = 2.5$  for largely separated wakes comparable to Figs. 12a and 13a and d. This consistency between the studies also applies to the buffet peak ( $St_c = 0.071$  in the present case vs.  $St_c = 0.075$  in [23]) and thus indicates identical governing mechanisms. At higher frequencies, we identify three additional dominant contributions, which most probably are the first harmonics to the previously discussed shedding peaks.

For shock downstream phases, the spectrum in Fig. 14b is qualitatively similar. As for the upstream case, we discern three spikes, which are, however shifted towards greater  $St_c$  compared to (a) ( $St_c = 2.16$ ,  $St_c = 2.74$ , and  $St_c = 3.02$ ). The corresponding harmonics are shifted accordingly, thus resulting in contributions at  $St_c = 4.13$ ,  $St_c = 5.24$ , and  $St_c = 6.17$ .

To consolidate these findings, we analyse the spectrograms of the same time signals in Fig. 15. In both the upstream (a) and downstream (b) cases, the characteristic low-frequency buffet peak (as well as the weaker disturbance from the light source) are visible. The spectral peaks associated with the presumed vortex shedding regime are stable in time: the peaks (centered around  $St_c = 2.17$  and  $St_c = 2.74$  for the upstream and downstream shock motion, respectively) persist over multiple buffet half-cycle durations  $T_{HC}$ .

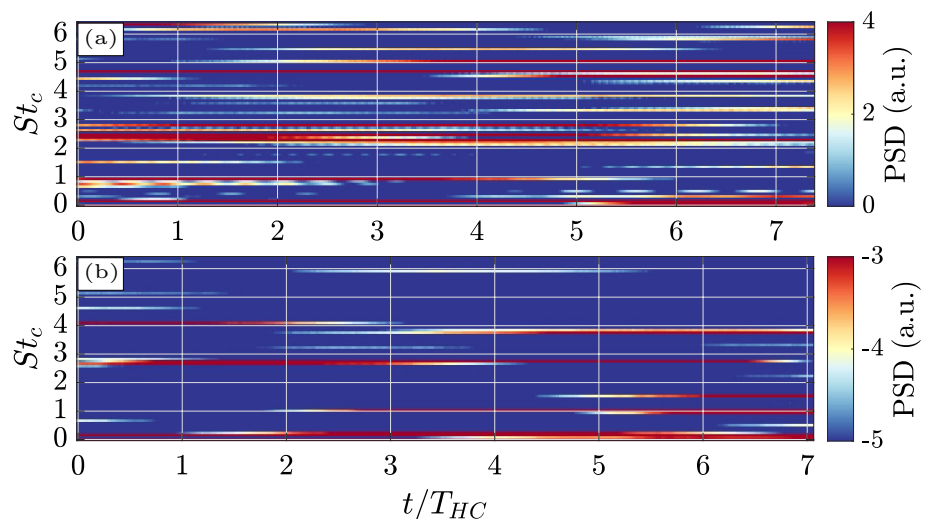
Considering the agreement between the present work and [23], as well as the frequency shift associated with the transition between upstream and downstream shock motion (which is in perfect agreement with the expected high-frequency/low-wavelength behavior), the identified main peaks in Fig. 14a and b can be attributed to the vortex-shedding process and the incipient formation of a von Kármán vortex street.

Also Zauner and Sandham [22] showed similar alternating large-scale structures (as shown in the present study in instantaneous  $v$  velocity (see Fig. 11) and vorticity plots (see Fig. 12) based on DMD modes representing both density and streamwise velocity in the wake field between  $x/c = 0.8$  and  $x/c = 2.0$ . The associated dynamics were centered around  $St_c = 1.8$ , which is a similar range as observed in the present case ( $St_c = 1.8$  to  $St_c = 3.0$ ). This agreement is satisfactory, considering the overall slightly different Strouhal number range found for the reported airfoil configuration in [22], which also includes deviant values for the buffet-related peak ( $St_c = 0.12$  vs.  $St_c = 0.07$ ).

### 3.4 Phase-averaged organization of the wake velocity field

The large-scale variation of the global flow topology associated with the buffet mode in the present 2D configuration has been discussed in Sect. 3.1. In good agreement with these prior findings, the streamwise velocity contours in Fig. 11 clearly indicate the same buffet-governed variation across the near wake domain. To allow for a conclusive statistical evaluation of the velocity field and the inherent turbulent quantities, we provide a phase-related description of the wake velocity field analogous to the discussion of the flow along the airfoil suction side following the procedure outlined in Sect. 2.3. Such representations are provided for

**Fig. 15** Spectrograms of vortex shedding in upstream (a) and downstream (b) phases, plotted over multiple buffet half-cycle durations  $T_{HC}$





the streamwise and vertical components in Figs. 16 and 17, respectively.

The contour maps in Fig. 16 show that the streamwise velocity maps vary periodically with the buffet cycle. The

low-velocity wake core fluctuates strongly, which is predominantly dictated by the respective location and direction of motion of the shock wave [34, 35]. The buffet mechanism leads to a pronounced variation of the vertical and

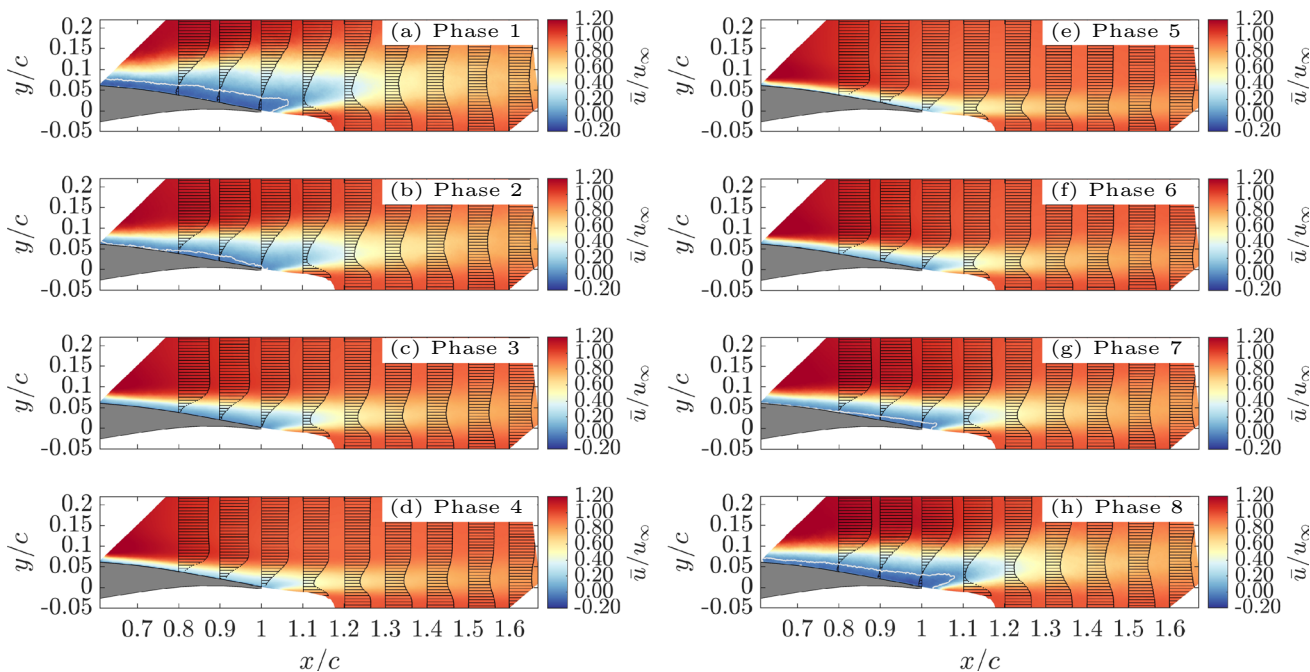


**Fig. 16** Phase-averaged streamwise velocity maps and profiles in the wake region for characteristic phases of the buffet cycle. Gray isolines  $\bar{u}/u_\infty = 0$  denote regions of reverse flow

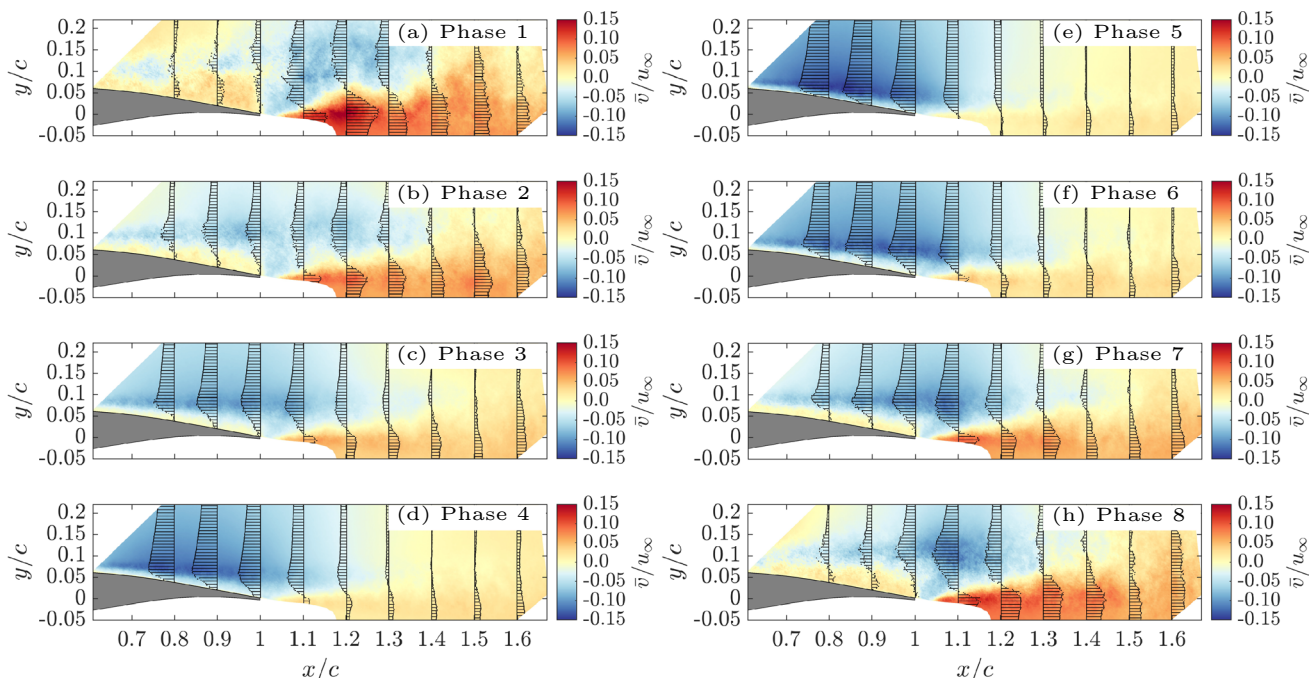


**Fig. 17** Phase-averaged vertical velocity maps and profiles for characteristic phases of the buffet cycle

streamwise extent of the velocity-deficit region, which is associated with an intense flapping motion of the separated shear layer [34, 35].

In the streamwise velocity magnitude, the greatest variation over the buffet cycle occurs with respect to its distribution the vertical direction (compare most extreme phases according to Fig. 16a and e). In the vertical component, dominant changes are most evident in the streamwise direction (see Fig. 17) and are attributed to the interplay between up- and downwash from both sides of the airfoil downstream of the trailing edge.

For the most upstream shock location (phase 1, see Fig. 16a), the severe flow separation and thickening of the separated shear layer overcompensate the curvature-related downwash in the rear part of the airfoil. Consequentially, a region of mild upwash results between  $x/c = 0.6$  and  $x/c = 1.0$ .

Immediately downstream of the trailing edge, the flow fields from the upper and lower sides coalesce, and the pressure side induces an upwards deflection with  $v/u_\infty \approx 0.1$  adjacent to a region of downwards flow above the trailing edge. This patch of negative vertical velocity persists until the chordwise station  $x/c \approx 1.4$ , beyond which the vertical component  $v$  is consistently positive. In phases with upstream shock locations, i.e. incipient downstream motion (phase 2) or final upstream motion (phase 8), the downwash along the airfoil suction side is still deficient and less pronounced compared to phases of widely attached flow (phases 4, 5, and 6).

Regarding the magnitude and spatial distribution, the organization of both the streamwise and vertical velocity maps in phases 3 and 7 are similar to the ensemble-averaged field shown in Fig. 9. In view of our central research objective, the quantification of the downstream wake influence,

these phases are most relevant to capture the implications on a downstream inflow in a temporal average sense.

To add to the discussion of phase-averaged streamwise velocities in the context of Fig. 16, we aim to quantify the buffet-induced momentum deficit and its impact in the near-wake region. Therefore, we compute the boundary-layer displacement thickness  $\delta_1$ , integrating the phase-averaged streamwise velocity profiles along  $y$  at different chordwise stations between  $x/c = 0.70$  and  $x/c = 1.0$  according to Eq. (2). As the accessible field of view is finite, the upper integration limit is replaced by the upper vertical limit of the domain  $y_{max}$ . Since the captured profiles extend into the external flow, Eq. (2) represents a reasonable estimate.

$$\delta_1 = \int_0^\infty \left(1 - \frac{u(x, y)}{u_\infty}\right) dy \approx \int_0^{y_{max}} \left(1 - \frac{u(x, y)}{u_\infty}\right) dy \quad (2)$$

Figure 18a evaluates  $\delta_1$  for each buffet phase as a function of  $x/c$ . All curves follow a similar trend: a progressive increase of  $\delta_1$  peaking at  $x/c \approx 0.95$ , followed by a substantial drop between  $x/c = 0.95$  and  $x/c = 1.0$ . This regained momentum is visible in slightly fuller velocity profiles in the boundary-layer region and is presumably attributed to turbulent mixing in the vicinity of the trailing edge. At most upstream locations  $x/c = 0.7$  and  $x/c = 0.75$ , we observe moderately negative  $\delta_1$  only for phases 3, 4, 5, and 6. Due to the displacement effect of the boundary layer, the  $\bar{u}$  component of those phases (Fig. 16) shows slight overspeed bumps just above the shear layer before the profiles level off towards free-stream conditions. This effect, along with the thin boundary layer, leads to a negative integral expression in Eq. (2).

We showed in Fig. 16 that phase 1 (most forward shock positions) features by far the greatest momentum deficit. In the transition from phase 1 ((a), most upstream) to phase 2

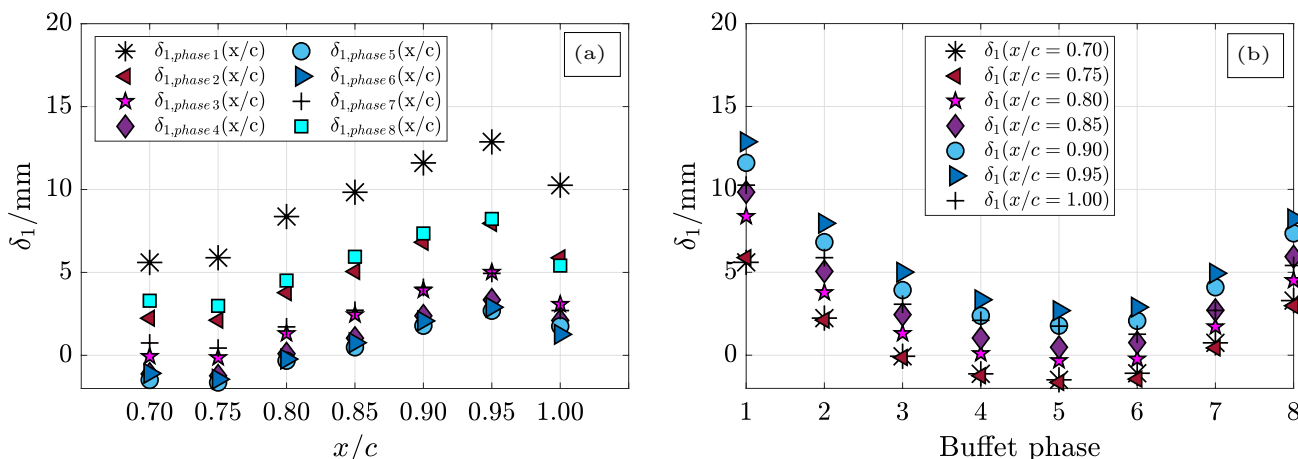


Fig. 18 Assessment of the boundary layer displacement thickness  $\delta_1$ , evaluated across different chordwise stations (a) and as a function of buffet phase (b)

(b), incipient downstream progression), the flow separation starts to recover in the front part of the airfoil, where the  $\bar{u} = 0$ -isoline and the airfoil contour practically collapse, while reverse flow persists in the rearward section. This trend is confirmed by the modified recirculation bubble and  $\bar{u}/u_\infty = 0$ -isolines in Fig. 16a and b. Also the computed values of  $\delta_1$  (Fig. 18a and b) depict this trend, most evidently in the vertical offset between the curves of phases 1 and 2 (Fig. 18a).

Confirming the qualitative trend of Fig. 16, phase 8 involves greater momentum deficits than phase 2: a distinct offset in  $\delta_1$  gradually decreases until the values collapse towards the trailing edge (compare curves of phase 2 and 8 between  $x/c = 0.7$  and  $x/c = 1.0$  in Fig. 18a).

While Fig. 18a shows the evolution of  $\delta_1$  along the airfoil chord, Fig. 18b depicts the influence of buffet phase. The evolution throughout a buffet cycle confirms that the quasi-periodic shock motion induces an equal reaction of the boundary layer in terms of momentum deficit. This results in a smooth decrease of  $\delta_1$  between phases 1 and 5, followed by the expected increase during the upstream shock motion in phases 6–8.

To complement the analysis of instantaneous vorticity maps in Fig. 12, we present the phase-averaged equivalent in Fig. 19, accompanied by profiles at selected locations  $x/c$ . This overview confirms preceding observations in the phase-averaged velocity fields (Figs. 16 and 17) regarding the clear separation between the strongly perturbed wake core region and the external flow field. Non-vanishing vorticity

is confined to the separated shear layer and wake area, whereas  $\omega_z$  tends toward zero in the non-rotational parts of the flow; this is most evident in phase 5 (see Fig. 19e). Some differences between the instantaneous (Fig. 12) and phase-averaged (Fig. 19) representations need to be taken into account when estimating the impact of disturbances imposed on a body placed in the wake. The instantaneous maps suggest only moderate dissipation of vorticity with increasing distance from the trailing edge, and peak vorticity pockets persist up to  $x/c \approx 1.6$ . The phase-averaged view on the other hand shows a much faster decay. In the instantaneous representation, persistent pockets of vorticity are visible in phase 1, which we use as a reference to assess the phase-average influence. In Fig. 19, greatest vorticity values occur slightly downstream of the trailing edge at chordwise station  $x/c = 1.1$ , along with a clear peak in the  $\omega_z$ -profiles (see for example Fig. 19a). In the downstream evolution, the  $\omega_z$ -profiles quickly flatten and spread across the vertical domain. Peak values have dropped by about 30 % at  $x/c = 1.2$ , and by more than 50 % at  $0.3 c$  downstream of the trailing edge. Beyond that location, the average vorticity values remain at relatively stable levels of  $\omega_{z,max} = 0.14 - 0.18$  up to  $x/c = 1.6$  across all displayed phases. Peak vorticity pockets survive far downstream of the airfoil trailing edge, whereas in a phase-averaged sense, values converge to less than  $0.2 \omega_{z,max}$  within half a chord length downstream of the trailing edge. We can thus corroborate the existence non-vanishing vorticity across all buffet phases, which suggests a persistent downstream impact.

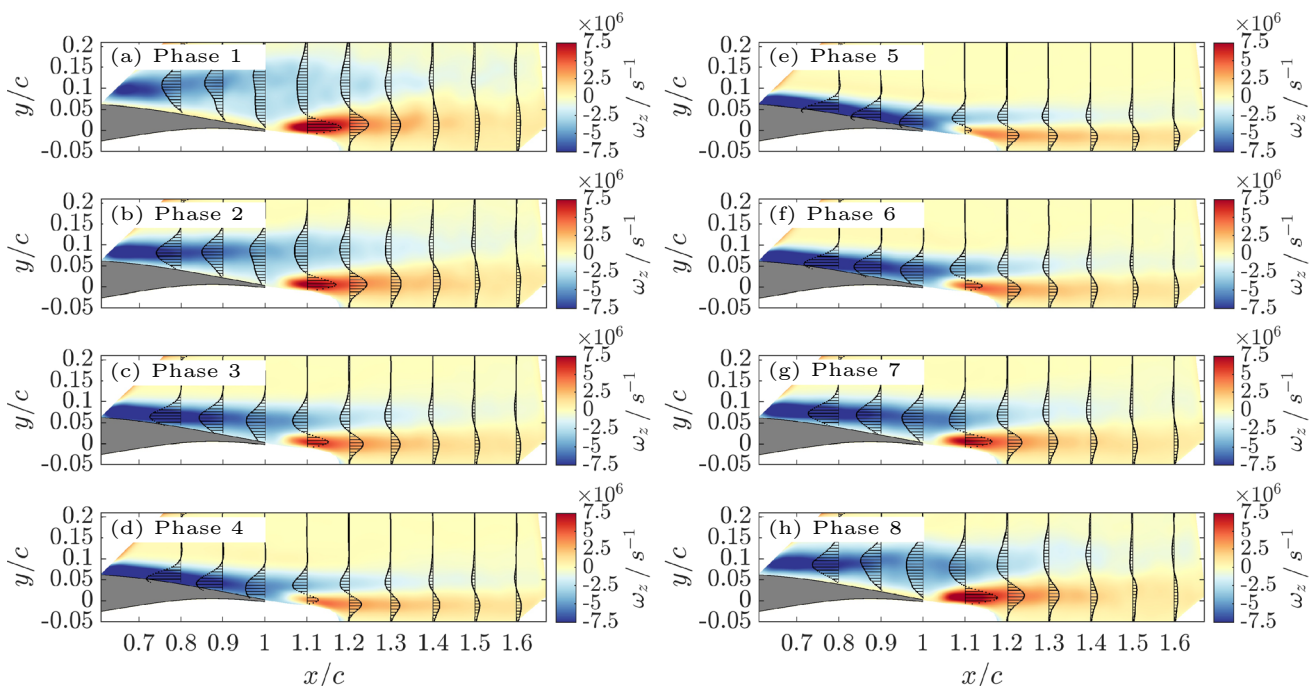


Fig. 19 Phase-averaged vorticity contour maps for characteristic phases of the buffet cycle



### 3.5 Evolution of turbulent quantities

Considering the strong variations of the turbulent wake across the different buffet phases, a more detailed analysis of the buffet-related perturbations is required. The streamwise and vertical turbulent quantities  $u_{rms}$  and  $v_{rms}$  as well as the Reynolds shear stresses  $Re_{uv}$  were computed for each phase individually (see Figs. 20 and 21) to assess their huge variations throughout the buffet cycle and further quantify their spatial structure.

The Reynolds shear stress contours in Fig. 20 are consistent with our prior findings [34] and agree with our observations above: intense turbulent mixing coincides with the incidents of large-scale flow separation, as is most clearly visible in phases 1 and 8 (Fig. 11b and p).

These effects are reflected in the shear-stress distributions of the same phases phases 1 (see Fig. 20a) and 8 (see Fig. 20h), whose respective maxima are located far above the TE at  $y/c = 0.1$  (phase 1) and  $y/c = 0.075$  (phase 8), and the wake influence is still noticeable until  $y/c = 0.2$  in both phases. Greatest maximum shear stress values of approx.  $-\overline{u'v'}/U_\infty^2 = 0.04$  occur in phase 1, which confirms the qualitative observations of the instantaneous vector field in Fig. 11a and b. As expected, the weakest shear stress of approx.  $-\overline{u'v'}/U_\infty^2 = 0.015$  occurs in phase 5, with a vertical peak location of  $y/c = 0.025$ . This immense variation within the buffet cycle further illustrates that the wake carries out a strong flapping motion, as discussed in

the context of Fig. 7 in Sect. 3.1 on the basis of the time history of the wake area estimate.

The streamwise and vertical turbulence components  $u_{rms}$  and  $v_{rms}$  show qualitatively similar distributions, although some distinct features are visible in the shapes of their profiles (see Fig. 21 left and right columns, respectively). Both quantities seem to emerge from two major source regions: from the suction-side shear layer downstream of the shock wave and from the lower side of the trailing edge. These contributions are reflected in the respective profiles near the airfoil trailing edge. At  $x/c = 1.1$ , as the flow of the suction and pressure sides coalesce for phases of far upstream shock locations (phases 1 and 8, see Fig. 21a, b, o, and p), the effect is most distinct: both  $u_{rms}$  and  $v_{rms}$  profiles exhibit two separate peak contributions (at  $y/c \approx 0.1$  and  $y/c \approx 0.0$ ), between which the turbulence intensity reduces. The distinctness of the peaks is much stronger for the streamwise  $u_{rms}$  component.  $u_{rms}$  is much more intense along the two wake main axes from the airfoil suction and pressure sides, whereas the vertical component is of more even magnitude across the width of the wake. This effect results in slightly M-shaped profiles for  $u_{rms}$ , e.g. at  $x/c \geq 1.2$ .

For  $u_{rms}$ , the contribution from the suction dominates: the overall levels and extent in the  $y$ -direction at the location of the trailing edge are greater than the minor contribution from the pressure side. The vertical fluctuations (right column of Fig. 21) are equally strong on either side. Furthermore, the wake contribution from the pressure side to the  $u_{rms}$  component decays much faster than the contribution to  $v_{rms}$  (at

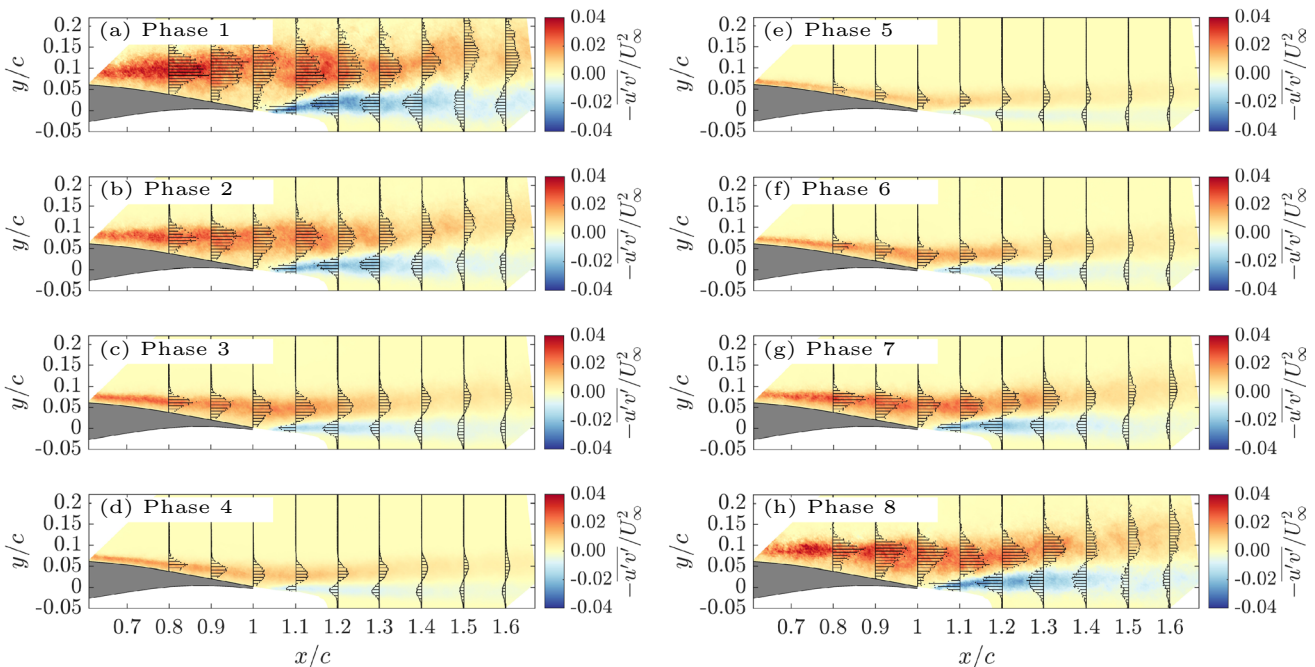


**Fig. 20** Reynolds shear stress  $Re_{uv}$  and its evolution during the buffet cycle

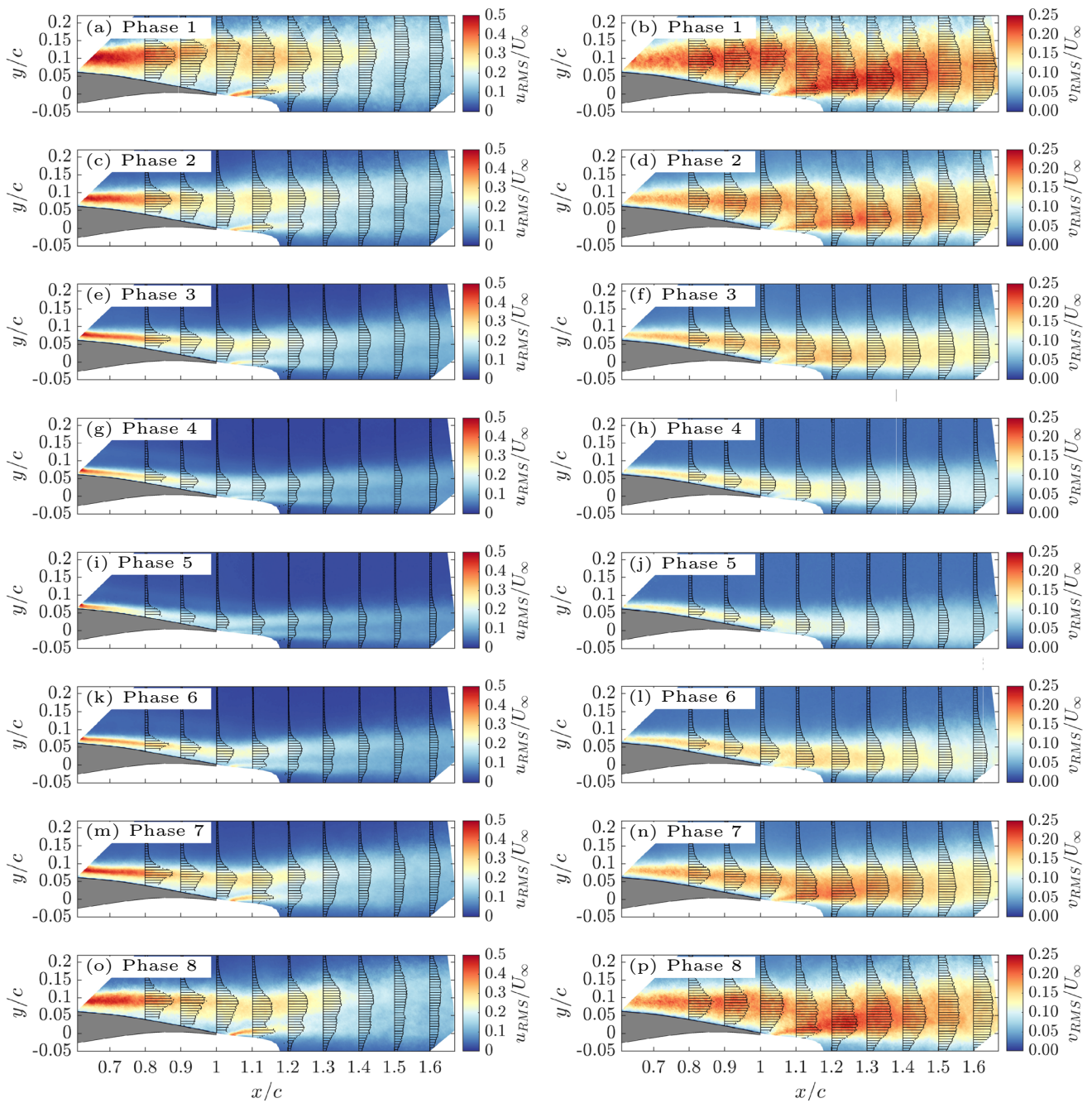


**Fig. 21** Overview of the turbulent quantities  $u_{rms}$  (left column) and  $v_{rms}$  (right column)

approx.  $x/c \leq 1.5$  in phase 1, whereas the contribution in  $v_{rms}$  has not yet decayed at  $x/c = 1.7$ ).

To provide an invariant measure of turbulent intensity, we show the turbulent kinetic energy (TKE) distribution for all buffet phases in Fig. 22. This quantity combines contributions of both horizontal and vertical fluctuation components. In comparison with the individual turbulent components (Fig. 21), the profile shapes of TKE exhibit greatest similarities with the streamwise component, showing characteristic

features such as pronounced M-shaped profiles in the near wake and in phases of strong separation. Overall, the streamwise fluctuation component seems to be the dominant influence.

To further characterize the influence of buffet phase on the turbulence structure, the anisotropy parameter  $\langle v \rangle / \langle u \rangle$  is given in Fig. 23. Some global observations are equally true across different phase bins. In the vicinity of the trailing edge (see e.g. stations  $x/c = 0.8$  and  $x/c = 1.0$ ),



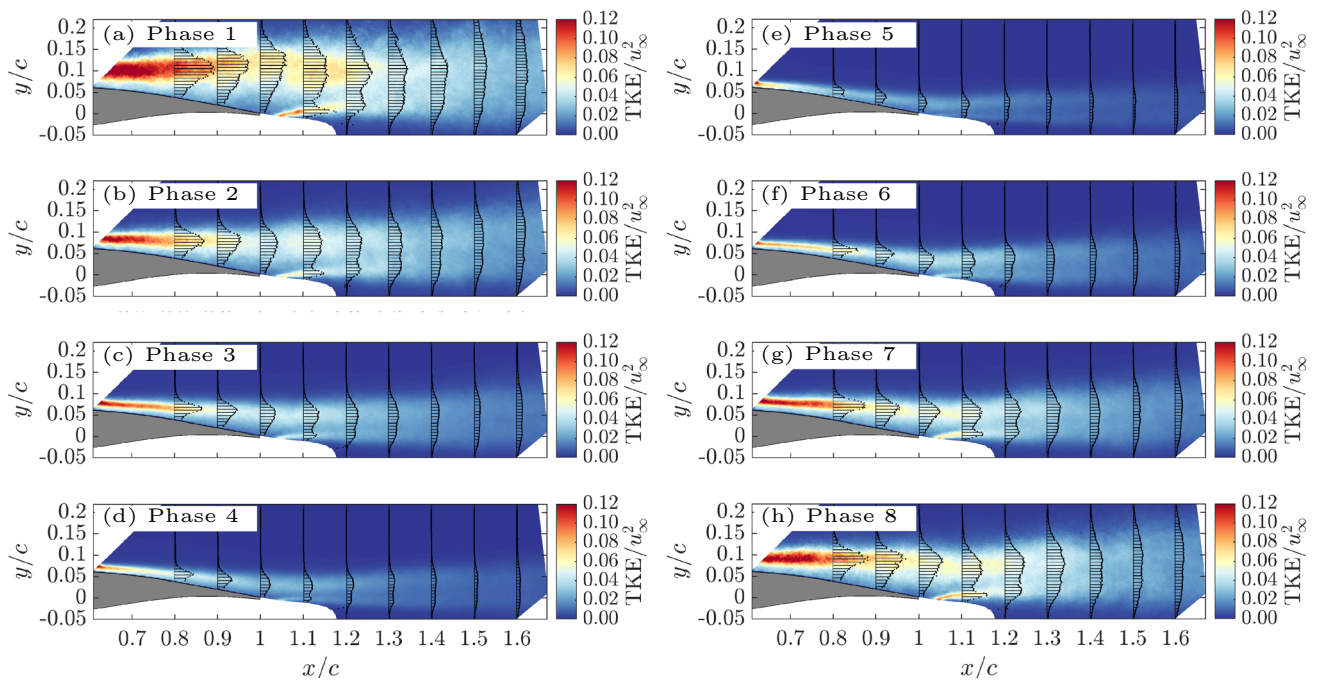


**Fig. 22** Evolution of turbulent kinetic energy over all buffet phases

the anisotropy remains almost constant close to the surface up to  $y/c = 0.05$ . These low values close to the wall can be attributed to the fact these regions are completely immersed in the separated boundary layer. Beyond a certain phase-dependent vertical location (e.g. at  $x/c = 1.0$  at  $y/c = 0.175$  in phase 1;  $y/c = 0.10$  in phase 3;  $y/c = 0.05$  in phase 5,  $y/c = 0.10$  in phase 7), the anisotropy increases precipitously. This results in a mostly flat plateau for phases of large separation and a distinct peak in phases of recovered flow (see for example Fig. 23d, e, and f). These peaks are related to the transition from the turbulent wake core to the upper shear layer; their occurrence consequently is in sync with the wake flapping motion. For reattached flow, e.g. phase 5, the upper shear layer is visible as a narrow streak of elevated anisotropy that moves towards the airfoil surface compared to phase 1, where the shear layer forms at the upper boundary of the captured FOV.

Similar trends can also be observed farther downstream in the wake region. At locations  $x/c = 1.2$  to  $x/c = 1.6$ , two bumps of local maxima are visible, again with varying  $y/c$  location depending on the buffet phase. With decreasing wake size, both local peaks shift closer to the airfoil surface due to the transition through the lower and upper shear layers. The largest anisotropy values at large  $y/c$  occur for intermediate phases 4 and 6. Overall, the anisotropy ratio, and thus the turbulence structure, vary strongly with buffet phase, and are modified periodically by the flapping of the wake and shear layers.

## 4 Conclusions

Transonic buffet strongly affects the aerodynamic performance of passenger aircraft. Due to large-scale shock oscillations, the flow on the suction side of the airfoil is subjected to large-scale intermittent flow separation. Via the wake of the airfoil or wing, also aerodynamic components downstream of the wing, e.g. the tail plane, are strongly affected by this intermittent flow field. To shed light on the flow structure and characteristics impinging on the tail plane, we analyzed the effects of the buffet cycle on the wake in detail.

The buffet-dominated flow fields along the OAT15A-airfoil suction side and in the airfoil wake were presented and discussed in a complementary way to elucidate the coupling between the shock-induced unsteadiness, the disturbances incited at the trailing edge, and the vortical structures in the wake. The flow field on the airfoil suction side undergoes a strong periodic and global variation throughout the buffet cycle, and also the wake (shown until  $x/c = 1.7$ ) is dominated by pronounced periodicity. Owing to the large-scale shock displacement coupled with an intermittent separation, the flow topology both along the airfoil and in the near wake is modified on a global scale. The associated fluctuations remain at a constantly high level throughout the entire studied domain ( $x/c = 1.7$ ) and are suspected to persist also farther downstream.

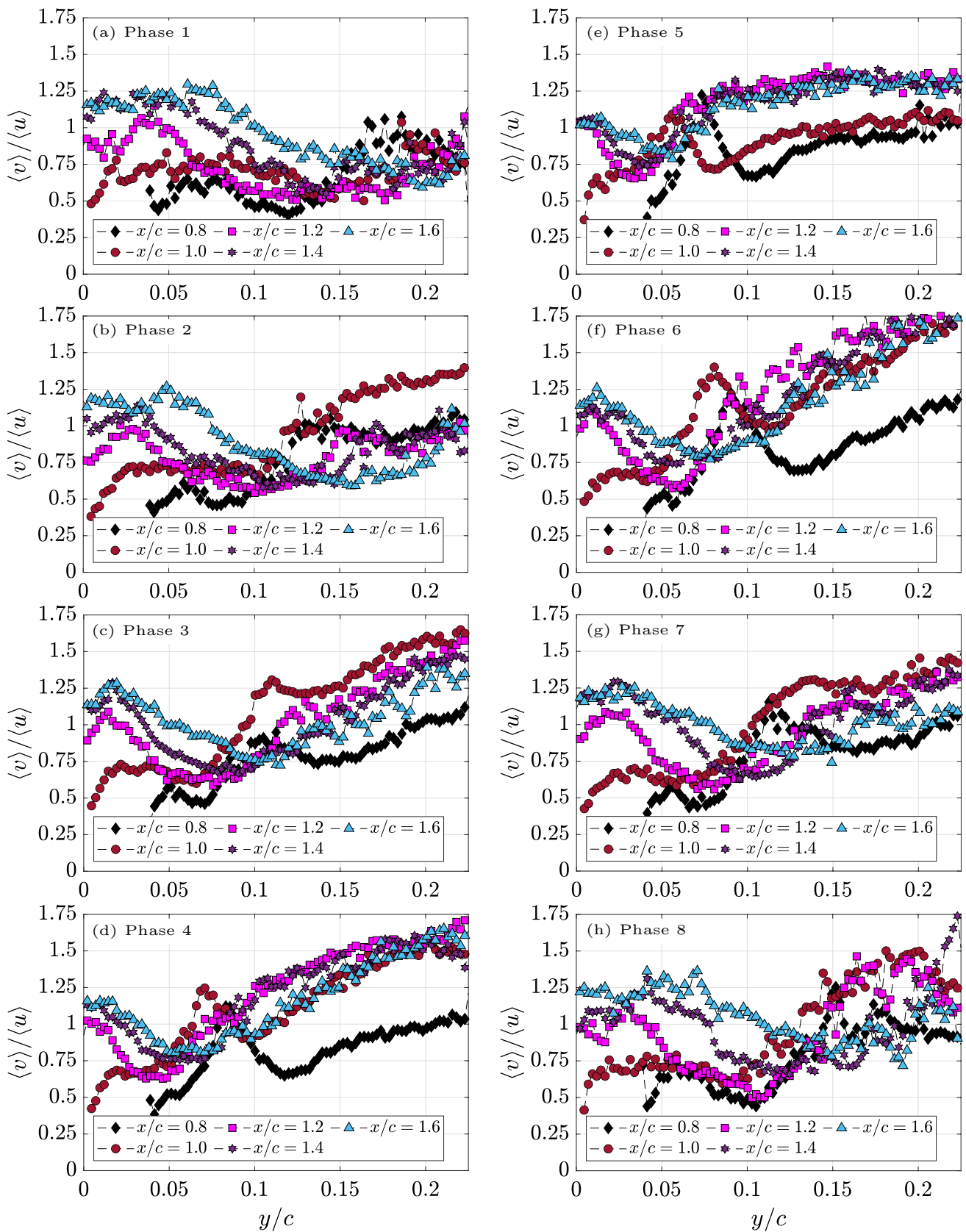


Fig. 23 Anisotropy parameter  $\langle v \rangle / \langle u \rangle$  evaluated at different chordwise stations for eight buffet phases

On the basis of phase-averaged streamwise velocity maps, we showed the flow's periodic variation, which is synchronized with the buffet cycle: the low-velocity wake core fluctuates strongly, dictated by the respective location and direction of motion of the shock wave. The wake is dominated by a pronounced variation of the vertical and streamwise extent of the velocity deficit associated with the flapping motion of the separated shear layer. Each buffet phase has a characteristic footprint of the flow topology, which is defined by the turbulent intensity and effective angular evolution of the main wake axis.

Downstream of the trailing edge, vortical structures form and are organized as large coherent streaks in phases where the wake is largest. They decrease substantially for phases of reattached flow. Positive vortical motion emanates at the lower edge of the wake and is intertwined with negative vorticity from the upper region. Consequently, Kármán vortex-street-like configurations form.

The low-frequency buffet unsteadiness modulates the vortex shedding, as it drastically modifies the circulation around and past the airfoil. The vortex shedding behavior strongly varies with the buffet phase, involving the governing shedding mechanism associated with frequencies one order of magnitude larger than those of the buffet mode ( $St = \mathcal{O}(1)$  and  $St = \mathcal{O}(0.1)$ , respectively). Phase-averaged spectral analyses revealed a characteristic low-frequency/high-wavelength behavior of the emerging vortices centered around  $St_c = 2.1$  in phases of an upstream traveling shock wave and large wakes. For phases of recovered flow and small wakes, high-frequency/low wavelength vortex shedding behavior at  $St_c = 2.7$  was observed. Those structures and associated frequencies will affect any downstream aerodynamic devices, such as the tail plane, on which the wake of the airfoil impinges. It is therefore to expect that the flow around the tail plane is also strongly periodic, with varying turbulent intensities associated with distinctly dominating peak frequencies in the range of the shock-buffet ( $St_c = 0.07$ ) and vortex shedding frequencies ( $St_c \approx 2 - 3$ ).

Vorticity is only weakly dissipated along the wake trajectory. Especially in phases with a large wake, peak vorticity values at the trailing edge persist up to  $x/c = 1.5$  and still maintain levels  $\approx 0.8 \times \omega_{z,max}$  at  $x/c = 1.6$ . These observations allow to assume a persistent wake influence also farther downstream than one chord length.

**Acknowledgements** The authors gratefully acknowledge the German Research Foundation (Deutsche Forschungsgemeinschaft DFG) for funding this work in the framework of the research unit FOR 2895 (project number 406435057). The authors thank ONERA for providing the OAT15A airfoil geometry for our wind tunnel model. We also gratefully acknowledge the contribution and support of Nick Capellmann and the workshop team of the Institute of Aerodynamics during the manufacturing process of the wind tunnel model.

**Funding** Open Access funding enabled and organized by Projekt DEAL. The research leading to these results received funding from the Deutsche Forschungsgemeinschaft DFG (German Research Foundation) in the framework of the research unit FOR 2895 (Unsteady flow and interaction phenomena at high-speed stall conditions), subproject TP6, under the project number 406435057. Open Access funding enabled and organized by Projekt DEAL.

## Declarations

**Conflict of interest** The authors have no conflict of interest to declare.

**Open Access** This article is licensed under a Creative Commons Attribution 4.0 International License, which permits use, sharing, adaptation, distribution and reproduction in any medium or format, as long as you give appropriate credit to the original author(s) and the source, provide a link to the Creative Commons licence, and indicate if changes were made. The images or other third party material in this article are included in the article's Creative Commons licence, unless indicated otherwise in a credit line to the material. If material is not included in the article's Creative Commons licence and your intended use is not permitted by statutory regulation or exceeds the permitted use, you will need to obtain permission directly from the copyright holder. To view a copy of this licence, visit <http://creativecommons.org/licenses/by/4.0/>.

## References

- McDevitt, J.B., Okuno, A.F.: Static and dynamic pressure measurements on a naca 0012 airfoil in the ames high Reynolds number facility. NASA Technical Paper 2485 (1985)
- Molton, P., Dandois, J., Lepage, A., Brunet, V., Bur, R.: Control of buffet phenomenon on a transonic swept wing. *AIAA J.* **51**(4), 761–772 (2013). <https://doi.org/10.2514/1.J051000>
- Jacquin, L., Molton, P., Deck, S., Maury, B., Soulevant, D.: Experimental study of shock oscillation over a transonic supercritical profile. *AIAA J.* **47**(9), 1985–1994 (2009). <https://doi.org/10.2514/1.30190>
- Iovnovich, M., Raveh, D.E.: Reynolds-averaged Navier-stokes study of the shock-buffet instability mechanism. *AIAA J.* **50**(4), 880–890 (2012). <https://doi.org/10.2514/1.J051329>
- Crouch, J., Garbaruk, A., Magidov, D., Travin, A.: Origin and structure of transonic buffet on airfoils. In: 5th AIAA Theoretical Fluid Mechanics Conference (2008). <https://doi.org/10.2514/6.2008-4233>
- Benoit, B., Legrain, I.: Buffeting prediction for transport aircraft applications based on unsteady pressure measurements. in: AIAA 5th Applied Aerodynamics Conference (1987). <https://doi.org/10.2514/6.1987-2356>
- Crouch, J.D., Garbaruk, A., Strelets, M.: Global instability in the onset of transonic-wing buffet. *J. Fluid Mech.* **881**, 3–22 (2019). <https://doi.org/10.1017/jfm.2019.748>
- Jacquin, L., Brion, V., Molton, P., Sipp, D., Dandois, J., Deck, S., Sartor, F., Coustols, E., Caruana, D.: Testing in aerodynamics research at onera: the example of the transonic buffet. *Aerospacelab* **12**, 1 (2016)
- Lee, B.H.K., Murty, H., Jiang, H.: Role of kutta waves on oscillatory shock motion on an airfoil. *AIAA J.* **32**(4), 789–796 (1994). <https://doi.org/10.2514/3.12054>
- Lee, B.H.K.: Oscillatory shock motion caused by transonic shock boundary-layer interaction. *AIAA J.* **28**(5), 942–944 (1990). <https://doi.org/10.2514/3.25144>

11. Tijdeman, H.: Investigation of the transonic flow around oscillating airfoils. Ph.D. thesis, Technical University of Delft, TU Delft (1977)
12. Xiao, Q., Tsai, H.M., Liu, F.: Numerical study of transonic buffet on a supercritical airfoil. *AIAA J.* **44**(3), 620–628 (2006). <https://doi.org/10.2514/1.16658>
13. Deck, S.: Numerical simulation of transonic buffet over a supercritical airfoil. *AIAA J.* **43**(7), 1556–1566 (2005). <https://doi.org/10.2514/1.9885>
14. Garnier, E., Deck, S., Armenio, V., Geurts, B., Fröhlich, J.: Direct and large-Eddy simulation VII, pp. 549–554. Springer, Dordrecht (2010)
15. Hartmann, A., Klaas, M., Schröder, W.: Time-resolved stereo piv measurements of shock-boundary layer interaction on a supercritical airfoil. *Exp Fluids* **52**, 591–604 (2012). <https://doi.org/10.1007/s00348-011-1074-6>
16. Hartmann, A., Feldhusen, A., Schröder, W.: On the interaction of shock waves and sound waves in transonic buffet flow. *Phys. Fluids* (2013). <https://doi.org/10.1063/1.4791603>
17. Giannelis, N.F., Vio, G.A., Levinski, O.: A review of recent developments in the understanding of transonic shock buffet. *Progress Aerosp. Sci.* **92**, 39–84 (2017). <https://doi.org/10.1016/j.paerosci.2017.05.004>
18. Crouch, J.D., Garbaruk, A., Magidov, D., Travin, A.: Origin of transonic buffet on aerofoils. *J. Fluid Mech.* **628**, 357–369 (2009). <https://doi.org/10.1017/S0022112009006673>
19. Gunasekaran, S., Curry, D.: On the wake properties of segmented trailing edge extensions. *Aerospace* (2018). <https://doi.org/10.3390/aerospace5030089>
20. Epstein, A.H., Gertz, J.B., Owen, P.R., Giles, M.B.: Vortex shedding in high-speed compressor blade wakes. *J. Propuls. Power* **4**(3), 236–244 (1988). <https://doi.org/10.2514/3.23054>
21. Alshabu, A., Olivier, H.: Unsteady wave phenomena on a supercritical airfoil. *AIAA J.* **46**(8), 2066–2073 (2008). <https://doi.org/10.2514/1.35516>
22. Zauner, M., Sandham, N.D.: Modal analysis of a laminar-flow airfoil under buffet conditions at  $re = 500,000$ . *Flow Turbul. Combust.* **104**, 509–532 (2020). <https://doi.org/10.1007/s10494-019-00087-z>
23. Szubert, D., Grossi, F., Jimenez-Garcia, A., Hoarau, Y., Hunt, J.C., Braza, M.: Shock-vortex shear-layer interaction in the transonic flow around a supercritical airfoil at high Reynolds number in buffet conditions. *J. Fluids Struct.* **55**, 276–302 (2015). <https://doi.org/10.1016/j.jfluidstructs.2015.03.005>
24. Franke, T.: Unsteady transonic flow around double-wedge profiles. *Exp. Fluids* **8**, 192–198 (1989). <https://doi.org/10.1007/BF00195795>
25. Paladini, E., Dandois, J., Sipp, D., Robinet, J.C.: Analysis and comparison of transonic buffet phenomenon over several three-dimensional wings. *AIAA J.* **57**(1), 379–396 (2019). <https://doi.org/10.2514/1.J056473>
26. Binion, T.W.: Potentials for pseudo-Reynolds number effects. *AGARDograph* **303** (1988)
27. McDevitt, J.B., Polek, T., Hand, L.: A new facility and technique for two-dimensional aerodynamic testing. In: 12th Aerodynamic Testing Conference (1982). <https://doi.org/10.2514/6.1982-608>
28. Nitzsche, J., Ringel, L.M., Kaiser, C., Hennings, H.: Fluid-mode flutter in plane transonic flows. In: IFASD 2019-International Forum on Aeroelasticity and Structural Dynamics (2019)
29. Gao, C., Zhang, W., Ye, Z.: Reduction of transonic buffet onset for a wing with activated elasticity. *Aerosp. Sci. Technol.* **77**, 670–676 (2018). <https://doi.org/10.1016/j.ast.2018.03.047>
30. Schardin, H.: Schlieren methods and their applications. *Ergebnisse der exakten Naturwissenschaften* **20** (1942)
31. Settles, G.: Schlieren and shadowgraph techniques: visualizing phenomena in transparent media. In: *Experimental fluid mechanics*. Springer, Berlin Heidelberg (2001). <https://doi.org/10.1007/978-3-642-56640-0>
32. Weinstein, L.M.: Large-field high-brightness focusing Schlieren system. *AIAA J.* **31**(7), 1250–1255 (1993). <https://doi.org/10.2514/3.11760>
33. Schauerte, C.J., Schreyer, A.M.: Design of a high-speed focusing Schlieren system for complex three-dimensional flows. In: 5th International Conference on Experimental Fluid Mechanics ICEFM 2018 Munich (2018)
34. Schauerte, C.J., Schreyer, A.M.: Characterization of shock buffet on a supercritical 2d airfoil in transonic flow. In: 20th International Symposium on Application of Laser and Imaging Techniques to Fluid Mechanics (2022)
35. Schauerte, C.J., Schreyer, A.M.: Experimental analysis of transonic buffet conditions on a two-dimensional supercritical airfoil. *AIAA J.* **61**(8), 3432–3448 (2023). <https://doi.org/10.2514/1.J062349>
36. Crouch, J., Garbaruk, A., Magidov, D.: Predicting the onset of flow unsteadiness based on global instability. *J. Comput. Phys.* **224**(2), 924–940 (2007). <https://doi.org/10.1016/j.jcp.2006.10.035>
37. Welch, P.: The use of fast Fourier transform for the estimation of power spectra: a method based on time averaging over short, modified periodograms. *IEEE Trans. Audio Electroacoust.* **15**(2), 70–73 (1967)

**Publisher's Note** Springer Nature remains neutral with regard to jurisdictional claims in published maps and institutional affiliations.